Final Technical Report for USGS Awards 06HQGR0205 and 06HQGR0206

3-D and 2-D Modeling of Strong Ground Motion from an M 7.0 Earthquake on the Salt Lake City Segment of the Wasatch Fault, Utah: Collaborative Research with San Diego State University and the University of Utah

September 1, 2006 - August 31, 2010

Principal Investigators:*

Kim B. Olsen
Dept of Geological Sciences, San Diego State University
5500 Campanile Dr, San Diego, CA 92182-1020
ph 619 594 2649, fax 619 594 4372
email kbolsen@sciences.sdsu.edu

James C. Pechmann
Dept of Geology and Geophysics, University of Utah
115 S 1460 East Room 383 FASB, Salt Lake City, UT 84112-0102
ph 801 581 3858, fax 801 585 5585
email pechmann@seis.utah.edu

* D. Roten, V.M. Cruz-Atienza, and H. Magistrale also contributed significantly to the work reported here.

Abstract

We predict ground motions in the Salt Lake Basin (SLB) during M 7 earthquakes on the Salt Lake City (SLC) segment of the Wasatch fault (WFSLC). First we generate a suite of realistic source representations by simulating the spontaneous rupture process on a planar, vertical fault with the staggered-grid split-node finite difference method. The initial distribution of shear stress is the sum of both a regional depth-dependent shear stress appropriate for a dipping, normal fault and a stochastically generated residual shear stress field associated with previous ruptures. The slip rate histories from the spontaneous rupture scenarios are projected onto a detailed 3D model geometry of the WFSLC that we developed based on geological observations. Next we simulate 0-1 Hz wave propagation from six source models with a 3D finite difference code, using the most recent version of the Wasatch Front Community Velocity Model. Horizontal spectral accelerations at two seconds (2s-SAs) reveal strong along-strike rupture direction effects for unilateral ruptures, as well as significant amplifications by the low-velocity sediments on the hanging wall side of the fault. For ruptures nucleating near the southern end of the segment we obtain 2s-SAs of up to 1.4 g near downtown SLC, caused by a combination of rupture direction and basin edge effects. Average 3s-SAs and 2s-SAs from the six scenarios are generally consistent with values predicted by four next-generation attenuation models.

We then generate broadband (BB, 0-10 Hz) ground motions for the M 7 earthquakes on the Salt Lake City segment of the Wasatch fault, Utah, which include the effects of nonlinear site response, by combining the 0-1 Hz finite-difference synthetics with high-frequency (1-10 Hz) S-to-S back-scattering operators. Average horizontal spectral accelerations at 5 and 10 Hz (0.2s-SAs and 0.1s-SAs, respectively) calculated from the linear BB synthetics exceed estimates from four recent ground motion prediction equations (GMPEs) at near-fault ($<$ 5 km) locations on the sediment generally by more than one standard deviation, but agree better with the GMPEs at larger rupture distances. The overprediction of the near-fault GMPE values is largely eliminated after accounting for near-surface soil nonlinearty with 1D simulations along E-W profiles in the Salt Lake basin, reducing the SAs from the simulations by up to 70%. The nonlinear simulations use a simple soil model based in part on published laboratory experiments on Bonneville clay samples.

Bibliography of all publications resulting from the work performed under the award

Roten, D., Olsen, K.B., Pechmann, J.C., Cruz-Atienza, V.M., and Magistrale, H. (2011). 3D Simulations of M 7 Earthquakes on the Wasatch fault, Utah, Part I: Long-period (0-1 Hz) Ground Motions, *Bull. Seism. Soc. Am.*, **101**, 5, 2045-2063.

Roten, D., Olsen, K.B., and Pechmann, J.C. (2011). 3-D Simulations of M 7 Earthquakes on the Wasatch fault, Utah, Part II: Broadband (0-10 Hz) Ground Motions and Nonlinear Soil Behavior, submitted to *Bull. Seism. Soc. Am.*

(The latter manuscript contains additional nonlinear modeling results done under 2011 NEHRP award G11AP20055).

Final Technical Report

Introduction

The Wasatch fault in northern and central Utah is a major normal fault that separates the Salt Lake Basin to the west from the Wasatch Range to the east. The Salt Lake City segment of the Wasatch fault (WFSLC) represents the most obvious source of seismic hazard to the Salt Lake basin (SLB), a major metropolitan area inhabited by more than a million people. Paleoseismological studies (Black *et al.*, 1995; McCalpin and Nishenko, 1996; McCalpin and Nelson, 2000) have shown that the WFSLC ruptures during large M∼7 surface faulting earthquakes with an average return interval of 1350±200 years, and that the last such event occurred approximately 1230±60 years B.P. Based on these findings, McCalpin and Nelson (2000) have estimated the probability of an M∼7 earthquake occurring during the next 100 years to be 16%; Wong *et al.* (2002a) have estimated that the probability for the next 50 years is 6 to 9%.

Worldwide there are few near-fault strong ground motion records from M≥6 normal-faulting earthquakes, and no records for M≥7 normal-faulting earthquakes (Chiou *et al.*, 2008; Campbell and Bozorgnia, 2008). As a result, there is a large uncertainty associated with the ground motions expected from future M 7 earthquakes on the WFSLC.

Adding to this uncertainty are the soft sediments of the SLB, which are more than 1km deep in some places. Such unconsolidated deposits may significantly amplify the seismic ground motion during large earthquakes, and contribute drastically to the loss of life and property, as has been demonstrated repeatedly during earthquakes elsewhere. Nonlinear soil behavior, on the other hand, may lead to a deamplification of strong ground motion, especially at higher frequencies (>1 Hz).

It is vital to gain a quantitative understanding of the ground motion expected from future large earthquakes on the WFSLC. In this study we address this issue by performing 0-1 Hz 3D finite difference (FD) simulations of wave propagation in the SLB based on a detailed velocity model, a realistic fault geometry, and rupture models derived from spontaneous rupture simulations.

The FD simulations presented in this paper are limited to frequencies of 1.0 Hz and lower. The synthetic ground motions are then extended to 10 Hz by combining our low-frequency (0-1 Hz) synthetics with a high-frequency (1-10 Hz) component based on scattering theory. We also perform simulations of nonlinear soil response, which typically becomes important at higher frequencies, for sites on three cross-basin profiles.

Background

The most recent studies of strong ground motion in the SLB were performed by Wong *et al.* (2002a), Wong *et al.* (2002b) and Solomon *et al.* (2004). They used a methodology that combines aspects of finite earthquake source modeling with the band limited white noise ground motion model, random vibration theory, ground motion attenuation relationships, and an equivalent-linear soil response calculation. Their results were consistent with previous studies by Adan and Rollins (1993) and Wong and Silva (1993), which accounted for near-surface site-effects in a similar manner. Wong *et al.* (2002a),Wong *et al.* (2002b) and Solomon *et al.* (2004) predicted 1.0 second spectral accelerations (1s-SAs) exceeding 1.3 g on the hanging wall side of the southern WFSLC, which they attributed to amplification by the relatively deep basin sediments there. Since all of these studies treated the site amplification in 1-D, they

could not account for effects caused by the 3D structure of the basin. However, numerous theoretical studies of seismic wave propagation in 2D and 3D structures have shown that basin walls play a major role in amplifying seismic waves (e.g., Bard and Bouchon, 1980a,b; Kawase, 1996; Olsen and Archuleta, 1996; Olsen *et al.*, 2009). Evidence for basin-edge generated waves has also been found in many weak ground motion records (e.g., Field, 1996; Frankel *et al.*, 2001; Cornou *et al.*, 2003; Roten *et al.*, 2008).

The important influence of the Salt Lake basin walls on seismic response was first reported by Benz and Smith (1988), Murphy *et al.* (1988), and Hill *et al.* (1990) based on 2D numerical simulations. Increases in computational power allowed Olsen *et al.* (1995), Olsen and Schuster (1995) and Olsen *et al.* (1996) to extend the numerical simulations to 3D. All of these 2D and 3D studies revealed large spectral amplifications in the modeled frequency range ($<$ 1.2-2.7 Hz), but they used rather simple models of the SLB and constrained the minimum shear-wave velocity to 410–2020 m·s^{-1} due to limitations in computational resources. A further limitation of these early numerical simulations was the representation of the seismic sources, which were modeled as horizontally or vertically incident plane waves, line or point sources, or 2D normal faulting earthquakes with uniform displacement.

More recently O'Connell *et al.* (2007) used a 3D finite element method to simulate spontaneous rupture on dipping faults. They also studied the effect of a bimaterial contrast across the fault by modeling the Teton normal fault in Wyoming, which, like the Wasatch fault, forms a boundary between bedrock on the footwall side and sediments on the hanging wall side. The simulations of O'Connell *et al.* (2007), which were performed in the frequency band 0–1 Hz, produced the highest peak ground velocities on the lower-velocity sediments on the hanging wall side of the fault. This result is qualitatively in agreement with the findings of Wong *et al.* (2002a), Wong *et al.* (2002b) and Solomon *et al.* (2004) for the southern WFSLC, where they predicted the highest 1s-SAs on the hanging wall side. But farther north along the central WFSLC, where there are sediments on both sides of the fault, Wong *et al.* (2002a) and Wong *et al.* (2002b) predicted the largest 1s-SAs (1.1 to $>$ 1.3 g) to be on the footwall side of the fault. The simulations of O'Connell *et al.* (2007) did not predict such amplifications on the footwall side, since sediments were only present on the hanging-wall side in their velocity model. These results demonstrate the need to perform realistic 3D numerical simulations using on an accurate velocity model of the SLB and a detailed source representation in order to predict ground motions during future M$\sim$7 earthquakes on the WFSLC.

Even the fastest supercomputers available today cannot deterministically simulate ground motion for the whole 0-10 Hz frequency range that is relevant for engineering. For this reason broadband (BB) methods have been developed which combine deterministic low-frequency (LF) ground motions with a high-frequency (HF) component to generate synthetic seismograms for the entire frequency range of engineering interest. A number of methods use stochastic seismograms to generate the HF component of the signal (e.g. Pitarka *et al.*, 2000; Mena *et al.*, 2006). Other methods incorporate the physics of wave scattering at frequencies above 1 Hz to simulate the HF ground motions (e.g. Zeng *et al.*, 1995; Hartzell *et al.*, 2005). Mai *et al.* (2010) combined HF (1-10 Hz) S-to-S back-scattering seismograms with LF (0-1 Hz) deterministic seismograms for the 1994 Northridge earthquake, and found that the resulting broadband synthetics were consistent with observations for the modeled frequency range. Mena *et al.* (2010) developed the method further by incorporating dynamically consistent source-time functions and accounting for finite-fault effects in the computation of the HF waveforms. Their method also includes corrections for local site effects that use frequency- and amplitude-dependent amplification functions (Borcherdt, 1994).

Deterministic 3-D LF simulations typically do not take soil nonlinearity into account,

since this effect is not very important at frequencies below 1 Hz. For the HF component of the ground motion, however, non-linear soil behavior may become an important factor during strong earthquakes. 0–10 Hz simulations of wave propagation in nonlinear media are primarily limited to 1-D (e.g. Hartzell *et al.*, 2004) and 2-D (e.g. Bonilla *et al.*, 2006). In geotechnical engineering it is standard practice to apply an equivalent linear 1-D model (e.g. Schnabel *et al.*, 1972). It is well accepted that this physical model is limited to a certain strain level above which the soil behavior becomes very complex. In these cases a fully non-linear calculation needs to be performed in order to accurately estimate the soil response.

The most recent and complete studies predicting broadband ground motions for M 7 scenario earthquakes on the WFSLC were performed by Wong *et al.* (2002a) and Solomon *et al.* (2004), who produced maps of average expected peak ground acceleration (PGA) and spectral acceleration at periods of 0.2s and 1s (0.2s-SAs and 1s-SAs, respectively) in and around the SLB. To account for site effects and nonlinear soil behavior, Wong *et al.* (2002a) and Solomon *et al.* (2004) defined five generalized site response units and calculated 1-D amplification factors for each unit as a function of input PGA and unconsolidated sediment thickness. Shear modulus reduction and hysteretic damping were incorporated using an equivalent-linear formulation (Silva *et al.*, 1998). The M 7 scenario earthquake ground motion maps by Wong *et al.* (2002a) and Solomon *et al.* (2004) show the highest PGAs and 0.2s-SAs near the surface break on the footwall side in the central SLB and on the hanging wall side in the southern part of the SLB. These areas are covered by stiff gravel and sand deposits, which amplify the ground motions at higher frequencies. Sites on the hanging-wall side of the fault that are underlain by soft lacustrine and alluvial silts, clays, and sands exhibit lower ground motions due to damping by nonlinear soil response. For a period of 1s, as mentioned previously, Wong *et al.* (2002a) and Solomon *et al.* (2004) predict the largest ground motions at near-fault sites on deep hanging-wall sediments in the southern SLB as well as on shallow footwall sediments in the central SLB (up to 1.3-1.5g).

The results of Wong *et al.* (2002a) and Solomon *et al.* (2004) suggest that the simulated ground motion pattern changes at higher frequencies during strong ground motion, as they predict the largest PGAs and 0.2s-SAs on the footwall in the central SLB. However, studies of site amplification from weak motion records of nuclear explosions in the period range 0.2s-0.7s (e.g. Williams *et al.*, 1993) found the highest amplification on the hanging-wall side of the fault, where the sediments are deepest. This discrepancy is likely related to nonlinear damping in the soil during strong ground motion. The purpose of this study is to produce BB synthetics based on the 0-1 Hz M7 Wasatch fault scenario ground motion simulations, and including nonlinear soil response, in order to produce ground motion synthetics useful for structural engineers and to allow a direct comparison with the results of Wong *et al.* (2002a) and Solomon *et al.* (2004).

Geophysical model and fault geometry

We use the Wasatch fault community velocity model (WFCVM version 3c, Magistrale *et al.*, 2009) for our simulations. The model includes detailed site response units based on surficial geology and shallow shear wave data (McDonald and Ashland, 2008) atop rule-based representations of basins along the Wasatch front, all embedded in a 3D crust derived from sonic logs and seismic tomography. It is conceptually similar to the SCEC velocity model created for southern California (Magistrale *et al.*, 2000).

Since the Wasatch fault forms the boundary between the SLB deposits on the hanging wall side to the west and the bedrock on the footwall side to the east, the shallow geometry of

the WFSLC is already partly defined in the WFCVM. The fault structure in the WFCVM is mostly based on work of Bruhn *et al.* (1992), who modeled the near-surface dips of different fault sections of the WFSLC based on field measurements and the assumption that most fault sections intersect along lines that have the same azimuth as the slip vector, which is 240°. We used this fault model as a basis to generate a realistic 3D model of the WFSLC to ensure that the fault model is consistent with the geometry of the basins.

The surface trace of our WFSLC model (thick line in Fig. 1) follows the general trends of the mapped Holocene surface faulting on this segment, which consists of three en-echelon sections separated by left steps: the Warm Springs fault (WSF), the East Bench fault (EBF) and the Cottonwood section (CS; Fig. 1). North of downtown Salt Lake City (SLC) our fault model follows the easternmost of the two branches of the Warm Springs section of the fault, as this branch appears to be the primary branch. We connected the southern end of the Warm Springs fault to the northern end of the East Bench fault by a straight tearfault in order to keep the fault model contiguous. The dip of the tear fault (65°) was modeled using the same assumptions made by Bruhn *et al.* (1992). Further south near Holladay the WFSLC model bridges another gap in the known Holocene fault trace, using a connecting fault that dips 30° to the SSW as in the Bruhn *et al.* (1992) model. South of this connecting fault, our fault model follows the narrow zone of surface scarps along the Wasatch Range front until the WFSLC ends at the Traverse Mountains barrier (Machette *et al.*, 1991).

We extrapolated the shallow fault geometry to greater depth using a dip of 50° and a slip azimuth of 240°, consistent with the average values in the Bruhn *et al.* (1992) WFSLC model. As a result, the geometry of the surface trace of the fault is generally preserved with increasing depth. The grid lines in Figure 1 show the surface projection of the fault mesh with along-strike and along-dip distances in 1000 m contours. Down-dip distances were measured along the surface of the fault in the slip direction. Along-strike distances were defined on the surface trace of the fault and projected to greater depth in the slip direction. We consider our 3D WFSLC model to be plausible based on the available geological information. However, the details of this model are uncertain due to the lack of data on the fault geometry at depth and the connections, if any, across the two left steps in the surface trace. We chose to connect both stepovers with faults because published dynamic rupture models do not support rupture jumps across 2- to 4-km fault discontinuities, at least on dip-slip faults (Magistrale and Day, 1999). The simulated ground motions would likely be different if the ruptures did, in fact, jump across these stepovers.

Figure 2 (left) is a fence diagram showing the shear-wave velocity in the central SLB and the fault geometry. The unconsolidated and semiconsolidated deposits reach a combined thickness of more than 1000 m on the hanging wall side of the fault to the north, while the footwall side consists mostly of bedrock. In the central part of the area shown in Figure 2 the fault runs west of the mountain front, cutting through the low-velocity sediments. Consequently we also find unconsolidated sediments on the footwall side in this area, although the sediment thickness is much greater on the hanging wall side. Figure 2 (right) is a map showing the average shear-wave velocity in the top 30 meters, V_{S30}. In the northwestern part of the SLB on the hanging-wall side of the Warm Springs fault and East Bench fault, V_{S30} is mostly between 200 and 300 m·s^{-1}. The V_{S30} is generally higher on the hanging-wall side of the Cottonwood Section in the southern part of the SLB, where it ranges between 300 and 600 m·s^{-1}. In the sediments on the footwall side of the East Bench fault in the central SLB, the V_{S30} is between 400 and 700 m·s^{-1}. We find larger V_{S30} of more than 600 m·s^{-1} adjacent to the fault on the footwall side of the Warm Springs fault and Cottonwood section. The colormap in Figure 2 (right) saturates at 1000 m·s^{-1}, but we note that the V_{S30} in the bedrock is typically ∼1450

$\mathrm{m{\cdot}s^{-1}}$ everywhere.

Figure 2 (right) also shows the depth to the R_1 interface, which marks the transition from unconsolidated to semi-consolidated sediments (Magistrale *et al.*, 2008). In the northern part of the SLB, the unconsolidated sediments are typically more than 200 m deep, with a maximum depth of 710 m west of the WSF. The R_1 interface is shallower in the southern part of the SLB, where it is typically less than 200 m below the surface except in the Cottonwood Heights area.

Dynamic rupture modeling

In order to obtain a suite of realistic rupture models of M 7 earthquakes on the Wasatch fault we perform simulations of spontaneous rupture on a 43 km (along strike) $\times$ 21 km (downdip) fault with the staggered-grid split-node FD method (Dalguer and Day, 2007). Because the code is limited to rupture simulation on a planar, vertical fault we adopt a two-step process. In a first step, we simulate the dynamic rupture process on a planar, vertical fault embedded in a 1-D model representative of the structure on the hanging wall side of the fault. Then the moment-rate time histories obtained from the spontaneous rupture simulation on the fault are projected onto the irregular 3D fault model represented by the mesh in Figure 1. In the second step, we simulate the wave propagation resulting from this kinematic rupture model embedded in the heterogeneous 3D structure of the SLB.

We follow a method proposed by Dalguer and Mai (2008) to define depth-dependent initial shear and normal stress on the fault. In an extensional tectonic regime the major principal stress σ_1 coincides with the vertical stress and is equivalent to the gravitational load σ_v (Sibson, 1991):

$$\sigma_1(h) = \sigma_v(h) = \int_0^h \rho(z)\ g\ dz, \tag{1}$$

where ρ is the rock density, h is the depth and g is Earth's gravitational acceleration. The minor principal stress σ_3 is being lowered due to tectonic extension:

$$\sigma_3 = \sigma_1 - \Delta\sigma, \tag{2}$$

with $\Delta\sigma$ increasing linearly with depth, such that $\Delta\sigma = 0$ at the free surface and $\Delta\sigma = 50$ MPa at 15 km depth. The shear (τ_t) and normal (σ_n) tectonic stresses on a fault of dip θ are thus given by:

$$\tau_t = \frac{\sigma_1 - \sigma_3}{2}\sin(2\theta) \tag{3}$$

$$\sigma_n = \frac{\sigma_1 + \sigma_3}{2} + \frac{\sigma_1 - \sigma_3}{2}\cos(2\theta). \tag{4}$$

The frictional strength on the fault obeys Coulomb friction and is defined as

$$\tau_c = C + \mu\sigma_n' = C + \mu(\sigma_n + p) \tag{5}$$

where C is the cohesive strength of the fault, and p is the hydrostatic pressure, which increases linearly with depth. The friction coefficient μ is described by a slip-weakening model:

$$\mu(l) = \begin{cases} \mu_s - (\mu_s - \mu_d)\ l/d_0 & \text{if } l < d_0 \\ \mu_d & \text{if } l \geq d_0, \end{cases} \tag{6}$$

where l is slip. We used a cohesion C of 1 MPa, a static friction coefficient μ_s of 0.67, and a critical slip displacement d_0 of 0.20 m. The dynamic friction coefficient μ_d was set to 0.57 for rupture models A and C and to 0.54 for rupture models B and D. This selection of parameters was found to generate generally sub-shear rupture propagation and a slip distribution reasonable for an M 7 normal faulting earthquake in terms of the average and maximum slip (Wells and Coppersmith, 1994).

We generated a heterogeneous stress field τ_r (Ripperger *et al.*, 2007), with a spectral decay that is compatible with seismological observations, using a fractal model with a dimension D of 2.5 and a corner wavenumber k_c of 0.125 km^{-1} (Mai and Beroza, 2002). Since the initial shear stress on the fault τ_0 is the combination of both the tectonic and residual stress components, we generated τ_0 by simply adding τ_t and τ_r so that its values are bounded by the static and dynamic fault strengths for all depths (Fig. 3) and such that the maximum shear stress reaches the static yield strength at a single point on the fault (Dalguer and Mai, 2008). Therefore, the location of the nucleation patch is predetermined by the location of the maximum in the random stress field. The initial shear stress was raised to 0.44% above the static failure stress inside the nucleation patch (diameter 3–6 km) in order to achieve stable sliding. Figure 3 (left panel) shows the initial normal stress σ_n and the initial shear stress τ_0 on the fault for rupture model B.

To emulate velocity strengthening in the shallow part of the crust d_0 was increased from 0.2 m to 1.0 m in the top 4 km using a cosine taper. Similarly, μ_d was raised to a higher value than μ_s in the top 2 km of the crust, and tapered linearly between 2 km and 4km depth (right panel in Fig. 3). Additionally, the shear stress τ_0 was tapered to zero at the free surface starting at 2 km depth using a ramp function. Due to the depth-dependent effective normal stress both the static (τ_{cs}) and dynamic (τ_{cd}) failure stresses

$$\tau_{cs} = C + \mu_s \cdot \sigma_n' \qquad \text{and} \qquad \tau_{cd} = C + \mu_d \cdot \sigma_n' \tag{7}$$

increase continuously with depth. Therefore, the dynamic stress drop $\Delta\tau = \tau_0 - \tau_{cd}$ as well as the strength excess $\tau_{cs} - \tau_0$ also increase with depth (center panel in Fig. 3). The average stress drop in our four rupture models varies between 3.5 and 3.75 MPa.

The spontaneous rupture simulations were performed on a $63 \times 50 \times 40$ km^3 mesh with a spatial discretization of 100 m. Figure 4 shows the final slip, rupture time and peak slip rates on the fault obtained for the four rupture models. The slip rates in each of the four rupture models were multiplied with a factor near one to scale the final slip to a value consistent with a M_w 7.0 earthquake.

Both rupture models A and B nucleate in the lower left corner and propagate towards the right and towards the free surface, with the highest final slip and peak slip rates occurring on the right-half of the fault. Rupture model C nucleates in the central part of the fault at approximately 10 km depth, while rupture model D has a deep, central hypocenter. In all rupture models peak slip rates are highest in the deeper part of the fault, where they are up to 2 m·s^{-1}. Despite the emulated velocity strengthening in the shallow structure, slip rates of up to 1 m·s^{-1} are reached close to the free surface for rupture models A and B. Rupture model C with its central, shallow hypocenter produces the lowest peak slip rates near the free surface, likely due to the minimal up-dip directivity for this model.

Rupture models A and B were mirrored laterally to analyse the effects of different rupture propagation directions on the the resulting ground motions. Figure 1 shows the hypocenter locations after the planar rupture models were mapped onto the irregular fault geometry, with rupture models A' and B' referring to the laterally mirrored rupture models. The distribution of hypocenters was chosen to represent spots where a future M 7 earthquake is likely to

nucleate. We placed five of our six hypocenter locations at 14-16 km depth below the surface, as normal-faulting earthquakes tend to nucleate near the brittle-ductile transition zone and then propagate upwards (e.g. Smith and Arabasz, 1991; Mai *et al.*, 2005). To analyze the influence of hypocenter depth on ground motions we included scenario C, which nucleates at an intermediate depth of 7 km below the surface. Bruhn *et al.* (1992) proposed two potential sites for rupture initiation, both of which they interpreted as non-conservative slip barriers (in the sense that the slip vector changes across the barrier): one at the southern end of the WFSLC, where there is a sharp bend in the fault, and the other near the center of the WFSLC, where there is a left step in the mapped surface trace and an intersection with an older branch of the fault. We also considered hypocenters along the part of the WFSLC north of the downtown SLC tear fault, as Bruhn *et al.* (1992) interpreted this area as a third non-conservative barrier. Therefore, our ensemble of rupture scenarios includes models A and B initiating near the northern end, models A' and B' nucleating near the southern end, and models C and D starting near the central barrier (Fig. 1). Note that all of our initiation points are located at irregularities in the fault surface.

Our ensemble of four dynamic rupture models is based on a relatively small subset of possible parameterizations. For example, we selected a fractal model to generate the stochastic component of the initial stress distribution for all of the dynamic simulations. Mai and Beroza (2002) show that the fractal model describes the power spectrum of published slip distributions equally as well as von Karman and exponential autocorrelation functions, at least for faults with small aspect ratios. While there are many studies recommending self-similar, fractal or von Karman stress distributions based on the spectral behavior of slip (e.g. Guatteri *et al.*, 2003; Mai and Beroza, 2002; Ripperger *et al.*, 2007; Schmedes *et al.*, 2010), we are not aware of any studies that recommend a specific distribution based directly on observed ground motions. Ripperger *et al.* (2008) suggest that the inter-event variability of ground motion is dominated by the effects of differing hypocenter locations and that the details of the heterogeneous stress distribution are of lesser importance. In our study the hypocenters are varied and selected from plausible nucleation points on the fault.

A further limitation is that all of our rupture models are based on a simple slip-weakening law (eq. 6), which has been used extensively in both numerical and observational studies (e.g. Andrews, 1976; Madariaga *et al.*, 1998; Fukuyama *et al.*, 2003; Cruz-Atienza *et al.*, 2009). However, it is known that laboratory observations are better explained with a rate-and-state variable friction law (e.g. Scholz, 1998), which describes the dependency of the friction coefficient on slip velocity (i.e. velocity strengthening or velocity weakening). Many studies support the presence of a velocity strengthening layer near the surface (e.g. Day and Ely, 2002; Somerville and Pitarka, 2006; Dalguer *et al.*, 2008; Kaneko *et al.*, 2008). Because the slip-weakening friction model implemented in our dynamic rupture code does not model rate-and-state friction directly, we have emulated the velocity strengthening layer in the crust by adjusting μ_d and d_0 as described earlier in this section.

Kinematic rupture models

We generated six kinematic source models from the spontaneous rupture simulation results. While the wave propagation simulations are performed with a grid step of 40 m, we discretized the WFSLC model on an 80 m grid to limit the size of the moment-rate files. For each subfault on the discretized fault model, the moment-rate time histories were computed using the following procedure:

i. We use the along-strike and down-dip position (contour lines in Fig. 1) to find the corresponding location in the planar rupture model.

ii. The slip-rate time histories for that location in the along-strike direction x_n and along-dip direction z_n (where the timestep $n = t_0 \ \ldots \ t_n$) are extracted from the spontaneous rupture results using a 2D spline interpolation (Press *et al.*, 2007).

iii. A 3$^{\text{rd}}$ order, one-pass Butterworth lowpass filter with a corner frequency of 1.2 Hz is applied to x_n and z_n. The slip-rate time histories are resampled to the desired temporal discretization Δt using a linear interpolation.

iv. We define the "along-dip" slip direction as a unit vector $\mathbf{U}_{\parallel}$, which has an azimuth of 240° (Bruhn *et al.*, 1992) and is parallel to the local surface of the irregular fault. $\mathbf{U}_{\parallel}$ is multiplied by the sliprate z_n, to form the "along-dip" component $\mathbf{S}^n_{\parallel}$ of the sliprate time series.

v. We calculate the direction of unit vector $\mathbf{U}_{\perp}$, which is perpendicular to $\mathbf{U}_{\parallel}$ and parallel to the local fault surface, pointing towards the strike direction. This vector is multiplied by x_n, to form the "along-strike" component $\mathbf{S}^n_{\perp}$ of the sliprate time series.

vi. We evaluate the time-dependent sliprate vector $\mathbf{S}^n = \mathbf{S}^n_{\parallel} + \mathbf{S}^n_{\perp}$, and the sliprate amplitude $|\mathbf{S}^n|$.

vii. We calculate the local strike ϕ_f and local dip θ on the irregular fault. The rake λ_n is defined as the angle between $\mathbf{S}^n$ and the strike direction. Therefore λ_n is time-dependent, allowing for rake rotation.

viii. We apply a ramp taper $k(\theta)$ in order to reduce slip on fault segments with unrealistically shallow dips for reasons explained below:

$$k(\theta) = \begin{cases} 0 & \text{if} \quad \theta < 25^\circ \\ \frac{(\theta - 25^\circ)}{5^\circ} & \text{if} \quad 25^\circ \geq \theta < 30^\circ \\ 1 & \text{if} \quad \theta \geq 30^\circ \end{cases} \tag{8}$$

ix. We compute the moment-rate tensor elements $T^{(n)}_{ij}$ from the strike ϕ_f, dip θ and rake λ_n for each time step n. The moment-rate tensor time series is scaled by the local shear modulus μ, the area of the subfault element A, and the slip rate amplitude:

$$T^{(n)}_{ij} = |\mathbf{S}^n| \ \mu \ A \ k(\theta) \ \left(n_i d^n_j + n_j d^n_i \right) \tag{9}$$

where $\hat{\mathbf{n}}$ and $\hat{\mathbf{d}}$ are unit vectors oriented normal to the fault and along the slip direction, respectively.

The taper $k(\theta)$ was introduced to eliminate slip on fault nodes where the dip is unintentionally low, as is the case for the shallow part of the stepover connection near Holladay (Fig. 1). Bruhn *et al.* (1992) assigned a dip of 30° degrees to this section using geometric modeling, which is the smallest dip anywhere in their WFSLC model. In the fault geometry provided by the WFCVM, the local dip in this area is even smaller (< 25°) for a few of the shallowest subfaults. Since the geometry of this fault segment is poorly constrained, normal faults generally steepen near the surface rather than flattening out, and there are no large fault scarps at the surface along the stepover, we decided to eliminate slip on the shallow part of the Holladay stepover connection using the dip-dependent taper. A second taper was applied to subfaults located inside a circular area of 3 km radius around the hypocenter to reduce artifacts produced by the artificial initiation of the rupture inside the nucleation patch.

The shear-modulus μ used to compute the moment rate in step (ix) differs, in general, from the shear-modulus in the 1-D model employed for the spontaneous rupture simulation. Consequently, the total seismic moment of the kinematic source deviates from the moment of the dynamic rupture models. To correct for this difference, the ground motions obtained from the wave propagation simulations are multiplied with a correction factor to obtain the target magnitude M_w=7.0.

Low-Frequency Ground Motions From M 7 Scenario Earthquakes

We simulated the wave propagation resulting from the six kinematic sources with the optimized, parallel AWP-ODC program (Cui *et al.*, 2010), which is based on the 3D velocity-stress staggered-grid FD code developed by Olsen (1994). Table 1 lists the key parameters used for the FD simulations. With a minimum shear-wave velocity $\min(v_s)$ of 200 m·s^{-1} and a grid step Δh of 40 m, frequencies of up to 1.0 Hz can be modeled using at least 5 gridpoints per wavelength. Surface topography was not included in the wave propagation model. We used a coarse-grained implementation of the memory variables for a constant-Q solid (Day and Bradley, 2001) and Q-velocity relations from Brocher (2006). 3D FD synthetic seismograms generated using this Q model and the WFCVM provide a satisfactory fit to data for a small earthquake below the Salt Lake Valley in the frequency range 0.5-1.0 Hz (Magistrale *et al.*, 2008).

Computation of horizontal spectral accelerations

As our simulations are limited to frequencies below 1 Hz, we analyze the spatial distribution of resulting ground motions by computing spectral accelerations for periods of 2 seconds (2s-SAs) and 3 seconds (3s-SAs). To combine the response spectra of the two horizontal components into a single measurement of ground shaking, we use the orientation-independent measure GMRotD50 defined by Boore *et al.* (2006). The GMRotD50 value is obtained by calculating the geometrical mean of the two horizonal-component spectral accelerations for a range of rotation angles θ, where $\theta = 0$, $\Delta\theta$, ..., $\pi/2$ and $\Delta\theta \approx 1^\circ$, and taking the median. Because with this approach the rotation angle θ corresponding to the median geometric mean depends on the period T of the response spectra, Boore *et al.* (2006) also define the measure GMRotI50, where the same rotation angle $\theta_{\min}$ is used for each period. $\theta_{\min}$ represents the rotation angle that minimizes extreme variations away from the median value over all periods. All next generation attenuation relationships (NGAs) use the GMRotI50 value. In our case, we are analyzing the spatial variability of the horizontal spectral acceleration for just a few selected periods between 1 and 10 seconds. Applications of the GMRotI50 value to recorded ground motions, however, typically use periods from 0.1 to 10 seconds. Therefore, we use the GMRotD50, rather than the GMRotI50 metrics, to compute rotation-independent spectral accelerations from both horizontal components.

Spectral accelerations at two seconds (2s-SAs)

Figure 5 shows 2s-SAs for the horizontal components for all six scenarios. Spectral accelerations for scenario A, where the rupture nucleates in the northern part of the SLB, exceed 0.6 g at many hanging-wall side locations, especially in the southern part of the SLB where they

exceed 0.8 g. Most of downtown SLC 2s-SAs remain below 0.5 g for this scenario. Nearly everywhere on the footwall, 2s-SAs are below 0.3 g. The pattern is significantly different for scenario A', which is based on the same rupture model, but mirrored laterally to make the rupture propagate from south to north. For this rupture direction, 2s-SAs in excess of 1 g appear in the Cottonwood Heights area and near central SLC. For this scenario we also observe values of more than 0.5 g on the footwall side of the fault in the northern half of the SLB, where there are thin, stiff, unconsolidated sediments. This comparison suggests that rupture direction has a big impact on the ground motions for ruptures nucleating near either end of the fault segment.

Effects of rupture direction are even more pronounced for scenarios B and B'. 2s-SAs for scenario B, with the rupture nucleating near the northern end of the WFSLC, peak southeast of Cottonwood Heights, where they exceed 0.8 g. In the central SLC area the 2s-SAs remain below 0.5 g for scenario B. Scenario B' with the mirrored source model, however, produces stronger ground motions with 2s-SAs up to 1.4 g near downtown SLC and on the hanging-wall side of the Warm Springs section.

The strong dependence of the 2s-SAs on rupture direction can be attributed, in part, to classical directivity. However, there are also other factors that contribute. The rupture direction effects can partly be traced back to the dynamic rupture models A and B (Fig. 4), with larger static slip and near-surface peak slip rates (more pronounced in model B than model A) at the end of the fault opposite the nucleation point. However, the generally higher 2s-SAs obtained for the two south-to-north rupturing scenarios A' and B', compared to the two north-to-south rupturing scenarios A and B, cannot be explained entirely as a source effect. This difference is likely influenced by the variation in depth and velocity of the unconsolidated sediments , which are deeper and lower velocity in the the northern part of the SLB than in the southern part (Fig. 2; Olsen *et al.*, 1995; McDonald and Ashland, 2008). The depth of interface R_1 exceeds 300 m west of the Warm Springs segment and around downtown SLC (Fig. 2 right). In the southern SLB, R_1 is located closer to the surface, mostly between 50 and 200m depth. However, the depth of R_1 exceeds 200 m in the Cottonwood Heights area, just west of where we obtained the highest 2s-SAs for scenarios A and B.

Since periods near 2 seconds are especially important for buildings with approximately 20 stories, we have indicated the locations of highrises ($\geq$20 story buildings) in the downtown SLC area (white squares in Figure 5). Even though highrises are located just north of the 'hot spot' southwest of the tearfault, they would still be subjected to spectral accelerations of more than 0.5 g in scenarios A' and B'. Bruhn *et al.* (1992) suggested that the southern end of the WFSLC may have been the most common position for repetitive rupture initiation during previous earthquakes, based on the fault segment geometry and on evidence that long-term deformation rates are highest at the southern barrier. Given this possibility, it certainly important to note that a south-to-north rupture yields significantly higher 2s-SAs in downtown SLC than a north-to-south rupture. However, the geology in that area is rather complex and the location of the tearfault is not well constrained. The use of a planar rupture model, which does not take the rupture dynamics caused by the irregular tearfault into account, represents another source of uncertainty for the simulated ground motion especially in the downtown SLC area.

Rupture model C, with its central, shallow (7.2 km) hypocenter, yields much lower average 2s-SAs than the other five scenarios (Fig. 5). The highest values (2s-SAs of up to 0.6 g) for this scenario occur near downtown SLC and on the hanging wall side of the Warm Springs fault segment. These relatively low 2s-SAs reflect the generally low peak slip rates in the near-surface area obtained from the spontaneous rupture simulation for rupture model C (Fig. 4).

Like rupture model C, rupture model D features a central hypocenter but at a greater depth (14.5 km below the surface). 2s-SAs from this scenario exceed 0.5 g in several areas on the hanging wall side of the fault (Fig. 5), with values of up to 1.0g north of SLC. The spatial distribution of ground motions represents an intermediate case between scenarios A and B, rupturing southwards, and scenarios A' and B', rupturing towards the north. It is striking that the 2s-SAs are up to twice as large as those from scenario C, which has a more shallow hypocenter. This difference illustrates a secondary rupture direction effect in the along-dip direction, with the deep hypocenter producing larger ground motions than the shallow hypocenter. This rupture direction effect is also evident in the spontaneous rupture simulation results, as peak slip rates in the uppermost 12 km, and especially in the uppermost 4 km, are larger for rupture model D than for rupture model C (Fig. 4).

Another striking observation that can be made from the simulated ground motions for all six scenarios is that the highest 2s-SAs are reached at some distance (1-2 km) from the surface rupture on the hanging wall side, rather than directly at the rupture. This result is consistent with the peak ground velocity (PGV) maps for the Teton fault published by O'Connell *et al.* (2007), where the highest PGVs occurred at distances of 1-4 km from the surface trace of the fault, also on the hanging-wall side.

Average 2s-SAs and 3s-SAs

Figure 6 (top) shows the geometric mean of the 2s-SAs and the standard deviation σ from all six scenarios. The average 2s-SAs exceed 0.3 g within a 5–10 km-wide zone on the hanging wall side of the fault, and reach up to 0.6 g close to downtown SLC and west of the Warm Springs section, as well as in the Cottonwood Heights area in the southern SLB. This distribution correlates partly with the depth to the R_1 interface (Fig. 2 left). The large average 2s-SAs in the northern SLB are due to the high values obtained from scenarios A' and B', which is reflected in the relatively large standard deviation for downtown SLC and the area west of the Warm Springs segment. The southern patch of high average 2s-SAs exhibits rather large accelerations in all of the six scenarios, and is characterized by a lower standard deviation. Two areas with large mean 2s-SAs are located southwest of a stepover: the small area southeast of downtown SLC, located south of the tearfault, and the Cottonwood Heights area southwest of the Holladay stepover. This result suggests that focusing effects caused by the concavely shaped fault geometry might contribute to the high average 2s-SAs in these areas (see, e.g. Olsen and Schuster, 1994).

Average 3s-SAs show a very similar spatial distribution, but values do not exceed 0.35 g for this period.

Comparison to next generation attenuation models

We evaluate the simulated ground motions by comparing the mean SAs from all six scenarios with values predicted by NGA models. We chose four of these recent attenuation relations: Boore and Atkinson (2008), Campbell and Bozorgnia (2008), Abrahamson and Silva (2008) and Chiou and Youngs (2008). For the remainder of this text, we will refer to these relations as BA08, CB08, AS08 and CY08, respectively. These four NGA relations use different source distance definitions. BA08 use only the Joyner-Boore distance, R_{JB}, which is defined as the closest distance to the surface projection of the fault rupture. In the case of the normal-faulting WFSLC, R_{JB} is zero for a large area inside the SLB (left panel in Fig. 7). CB08, AS08 and CY08 use both R_{JB} and the closest distance to the rupture surface, R_{Rup}. Additionally, AS08

and CY08 require R_x, which is defined as the shortest distance from a site to the top of the rupture (extended to infinity in both directions), measured perpendicular to the fault strike.

All of the NGA models use the average shear-wave velocity in the top 30 meters, V_{S30}. For the comparison we focus on the ground motions on the softest sediments on the hanging wall side, where the simulations yield the strongest ground motion. We chose all sites in the computational area where V_{S30} is between 200 and 300 m·s^{-1} in the velocity model, and evaluated the NGA predictions for V_{S30}=250 m·s^{-1}. We obtained V_{S30} in the computational model by interpolating from the value at the free surface, $v_s^{k=0}$, and at the first node 40 m below the surface, $v_s^{k=1}$. Highlighted patches in Figure 7 (left) show the areas that were used for the comparison with Boore and Atkinson (2008), and contour lines show $R_{\rm JB}$.

Spectral observations from the simulations were binned into 20 distance ranges, spaced logarithmically between 1 and 20 km. The bin centered at $R_{\rm JB}$=1 km includes $1.2{\cdot}10^6$ grid-points with $0 \leq R_{\rm JB} \leq 1$ km, and represents a larger sample size than the remaining bins, which contain between $1.4{\cdot}10^4$ and $2.3{\cdot}10^5$ grid points (Fig. 7). Geometric means for $R_{\rm JB} \leq$1 km exceed the values predicted by the BA08 relation by ∼25% for 3s-SAs and by ∼40% for 2s-SAs. At $R_{\rm JB}$ distances of 1 to 15 km, all of the 2s and 3s simulated mean SAs are within 25% of the BA08 predictions. It is noteworthy that the simulated mean 3s-SAs are higher for $R_{\rm JB}$s of 4 to 5.5 km than for $R_{\rm JB}$= 2 km. This observation could be explained by the relatively large average 3s-SAs 5 km northwest of the northwest edge of the rupture (Fig. 6), where most grid points with $R_{\rm JB} \approx 5$ km in the area of comparison are located.

In general, the agreement between the mean simulated 3s-SAs and 2s-SAs and the values predicted by the equation of BA08 is very favorable. The geometric standard deviation of 2s-SAs and 3s-SAs from the simulated ground motions is also quite close to the predicted values. This agreement suggests that our ensemble of six finite difference simulations adequately represents the variability in ground motions. However, we note that using the Joyner-Boore distance alone can be problematic for the WFSLC, since $R_{\rm JB}$=0 for a large area that shows a significant variability in the simulated ground motions.

For this reason, we performed a similar comparison for the area with $R_{\rm JB} = 0$ using the ground motion prediction equations by CB08, AS08 and CY08 as a function of $R_{\rm Rup}$. In order to remove the dependency of AS08 and CY08 on R_x for plotting purposes, we followed the OpenSHA (2010) approach by setting

$$\frac{R_{\rm Rup} - R_{\rm x}}{R_{\rm Rup}} \tag{10}$$

equal to its average value within the area of interest. Inside the area considered for the comparison ($R_{\rm JB}$=0, 200 m·s^{-1} $\leq V_{S30} \leq$ 300 m·s^{-1}) , this normalized difference between $R_{\rm Rup}$ and R_x (eq. 10) averages to -0.40±0.23 (standard deviation). It is negative as R_x is defined as positive on the hanging wall side. Additionally CB08 requires the parameter $Z_{2.5}$, which is defined as the depth where the shear-wave velocity reaches 2500 m·s^{-1}; we chose $Z_{2.5}$=2.71 km as an average value estimated from the WFSLC. AS08 and CY08 use the depth Z_1 to v_s=1000 m·s^{-1}. We evaluated AS08 and CY08 using the average of Z_1 in the selected area (highlighted patches in Fig. 8), which is 389 ± 95.4 m (standard deviation).

For rupture distances below 4 km, the average simulated 3s-SAs and 2s-SAs are generally within the range of values spanned by the CB08, AS08 and CY08 predictions and well within one standard deviation of all three models. For larger rupture distances the average simulated SAs fall below the values predicted by all three NGA models. At $R_{\rm Rup}$ ∼10 km, the simulated 3s-SAs and 2s-SAs are about one standard deviation below the NGA predictions. The saturation of the simulated 3s-SAs and 2s-SAs at small rupture distances is in agreement

with the NGA curves. The highest simulated average 3s-SAs are reached at rupture distances between 1.2 and 2.7 km, while the largest average 2s-SAs are encountered at $R_{\rm Rup}$ between 1.15 and 1.5 km. It is important to keep in mind that, as mentioned earlier, the data set used to determine the attenuation relations provides no direct constraints for M 7 normal-faulting earthquakes.

Simulated average ground motions on bedrock sites on the footwall tend to be much lower than those on hanging-wall sediments (Fig. 6). To see if the NGA models predict a similar trend we performed a comparison for all the sites on the footwall with V_{S30} above 1000 m·s^{-1} inside the computational domain (left panel in Fig. 9), excluding the absorbing boundaries. We evaluated the four NGA models using the average V_{S30} of 1443 m·s^{-1} inside the area of comparison. Since $R_{\rm JB} = R_{\rm Rup}$ on the footwall side, the predictions of BA08 can be directly compared with those of the other three relations. Additionally, we assumed that $R_x = R_{\rm Rup}$ on the footwall to simplify the comparisons with AS08 and CY08.

The central panels in Figure 9 compare simulated 3s-SAs and 2s-SAs with the BA08 and CB08 predictions. The simulated 3s-SAs agree well with the values from CB08 for rupture distances above 3 km. For smaller rupture distances, the simulated values are up to 30% lower than CB08, but still within one standard deviation. 3s-SAs predicted by BA08 are generally one standard deviation lower than the simulations. The comparison for 2s-SAs yields very similar results. AS08 and CY08 predict similar ground motions as CB08, and compare favorably with the simulated 3s-SAs and 2s-SAs (right panels in Fig. 9). We note that the simulated SAs tend to be below the NGA relations for $R_{\rm Rup} < 4$ km and $R_{\rm Rup} < 8$ km for 3s-SAs and 2s-SAs, respectively. Simulated SAs experience a sharp drop for $R_{\rm Rup} \approx 20$ km, which we attribute to the much smaller sample size in the last distance bin (bottom right panel in Fig. 9).

Methodology for Computing BB Ground Motions

In this section we generate 0-10 Hz broadband ground motion synthetics for the 6 M 7 Wasatch fault earthquake scenarios discussed earlier. We are following the method of Mai *et al.* (2010) and Mena *et al.* (2010) to calculate the HF component of ground motion. Additionally we calculate nonlinear soil response for ∼450 sites in the SLB with the nonlinear, anelastic hysteretic FD code NOAH (Bonilla *et al.*, 2005).

Generation of broadband synthetics

In the BB method of Mai *et al.* (2010), the generation of the HF part of the seismogram is based on multiple shear-to-shear (S-to-S) backscattering theory. Zeng *et al.* (1991) provide a compact integral solution of the scattered wave energy equation for an unbounded 3-D medium, which quantifies the energy envelope E of the S-to-S scattered waves:

$$E(\mathbf{r},t) = \frac{\delta\left(t-\frac{r}{v_s}\right)e^{-\eta v_s t}}{4\pi v_s r^2} + \sum_{n=1}^{2} E_n(\mathbf{r},t) + \int_{-\infty}^{+\infty} \frac{e^{i\Omega t}}{2\pi} d\Omega \cdot \int_0^{\infty} \frac{\left(\frac{\eta_s}{k}\right)^3 \left[\tan^{-1}\left(\frac{k}{\eta+i\Omega/v_s}\right)\right]^4 \sin(kr)}{2\pi^2 v_s r\left[1-\frac{\eta_s}{k}\tan^{-1}\left(\frac{k}{\eta+i\Omega/v_s}\right)\right]} dk. \quad (11)$$

In the above expression, $\mathbf{r}$ is the source-receiver vector, t is time and v_s is the average S-wave velocity between the source and the receiver. The total S-wave attenuation coefficient

$\eta = \eta_i + \eta_s$ contains the scattering coefficient η_s and the intrinsic attenuation coefficient η_i; we use $\eta_s = \eta_i = 0.03$ km^{-1} in this study. The first two terms in equation 11 represent time-domain solutions for the direct arrival and the first- and second-order scattered wave energy (E_1 and E_2, see Zeng *et al.*, 1991). The third term represents the sum of the higher-order ($n \geq 3$) scattered wave energy, where $i\Omega$ denotes the Fourier transform variable with respect to time, and k the wavenumber. Zeng (1993) shows that the wavefield of scattered P- and S-waves is dominated by multiple S-to-S back-scattered body waves described in equation 11. Scattered surface waves are not explicitly considered with this approach.

To generate a site-specific scattering Green's function, the code of Mai *et al.* (2010) generates a series of random scattering wavelets with uniformly distributed amplitudes between $\pm\sqrt{3}$, which assures a mean wave energy of unity (Zeng *et al.*, 1995). These wavelets are then multiplied with the envelope of the scattered wave energy (eq. 11), with P- and S-wave arrival times for each site computed from a 3-D raytracing method. For the raytracer we used the same velocity model as for the 3-D FD simulations, downsampled to a spatial resolution of 1 km. Additionally, the code models site-specific attenuation in the upper layers with a kappa coefficient, κ. For our BB simulations in the SLB, we used κ=0.03 s (Wong *et al.*, 2011).

Since the point source approximation by Mai *et al.* (2010) is not appropriate for modeling a M_w 7 event on the WFSLC, we employ the extended fault approximation developed by Mena *et al.* (2010) for the generation of BB synthetics. We divide the WFSLC fault model into 925 subfaults of 1 km^2 area each. The BB generator adds the contribution of each subfault to the total ground motion $A(t)$ based on the empirical Green's function method of Irikura and Kamae (1994):

$$A(t) = \sum_{i=1}^{N^2} (r/r_i)\,\mathrm{STF}(t - t_i) * C \cdot \mathrm{SGF}(t). \tag{12}$$

In this expression, r is the hypocentral distance, N^2 is the total number of subfaults, and r_i is the distance of the observation point to the i-th subfault. The operator $*$ indicates convolution. STF(t) is the source-time function, SGF(t) the scattering Green's function, and C is the stress-drop ratio between the small and large events. The time t_i accounts for the time delay for rupture propagation along the fault

$$t_i = \frac{r_i}{v_s} + \frac{\xi_i}{v_r}, \tag{13}$$

where ξ_i is the distance from the subfault to the hypocenter, v_s is the shear-wave velocity and v_r is the rupture velocity. Mena *et al.* (2010) employ a STF introduced by Dreger *et al.* (2007) due to its smooth spectrum, modified to include a healing phase.

The LF FD synthetics are combined with the HF scatterograms (maximum frequency 20 Hz) using a simultaneous amplitude- and phase-matching algorithm (Mai and Beroza, 2003). This approach finds the optimum matching frequency within a predefined frequency band and minimizes mismatches in both amplitude and phase. The matching frequency depends on the site and component. In this work we search for a matching frequency between 0.8 and 1.0 Hz, since our LF synthetics are limited to 1.0 Hz. We apply the scattering operators to LF synthetics at every 5th node on the surface of the computation grid. This results in a spatial resolution of 200 m and a grid dimension of 225$\times$ 300 nodes (67,500 sites), which allows us to generate SA and PGA maps with sufficient resolution.

Calculation of nonlinear soil response

We use the second-order accurate, staggered-grid 1-D finite difference code NOAH (Bonilla *et al.*, 2005) to model SH wave propagation in soil columns of 240 meters depth. The datum of 240 meters was chosen in order to include the structure above the R_1 interface, which marks the transition from unconsolidated to semiconsolidated sediments in the SLB (Hill *et al.*, 1990). The nonlinear simulations are performed for 540 sites, which are distributed evenly along three profiles across the SLB (Fig. 10) at 200 m intervals.

Soil model

Depending on the specification of soil parameters NOAH uses different models of nonlinearity. It is able to treat undrained conditions of effective stress using the multispring mechanism model introduced by Towhata and Ishihara (1985), and an extension of this model which treats cyclic mobility and soil dilatancy (Iai *et al.*, 1990b,a). This cyclic mobility model uses a relatively large number of variables (five dilatancy parameters), which need to be determined from laboratory tests that include pore pressure generation (e.g. Bonilla, 2001; Roten *et al.*, 2011). Because we only have laboratory data from one site in our computational area, we decided against simulating pore pressure generation in this study, and use the NOAH code for total stress analysis. In this configuration the multispring model gives the same result as a single element hyperbolic model following the Generalized Masing rules (Bonilla, 2000), and it is very similar to the nonlinear model "NOAHH" described in Hartzell *et al.* (2004).

In the hyperbolic model, the reduction of the shear modulus G with increasing strain γ_{xy} is described by

$$\frac{G}{G_0} = \frac{1}{1 + \frac{\gamma_{xy}}{\gamma_r}} \tag{14}$$

where G_0 is the shear modulus at low strain. The reference strain γ_r is defined as

$$\gamma_r = \frac{\tau_0}{G_0}, \tag{15}$$

where τ_0 is the maximum shear stress that the material can support in the initial state. The nonlinear relation between stress τ_{xy} and strain γ_{xy} is described by a backbone curve during initial loading (Fig. 11):

$$F_{\mathrm{bb}}(\gamma_{xy}) = \tau_0 \frac{\frac{\gamma_{xy}}{\gamma_r}}{1 + \left|\frac{\gamma_{xy}}{\gamma_r}\right|}. \tag{16}$$

Subsequent loading and unloading cycles are expressed as

$$\frac{\tau_{xy} - \tau_t}{\kappa_H} = F_{\mathrm{bb}}\left(\frac{\gamma_{xy} - \gamma_t}{\kappa_H}\right), \tag{17}$$

where the coordinates (γ_t, τ_t) denote the reversal points in the strain-stress space (Fig. 11). The hysteresis scale factor κ_H controls the shape of the loop (Bonilla *et al.*, 1998), and κ_H equals 2 in the original Masing (1926) formulation. In the extended Masing rules (e.g. Pyke, 1979; Vucetic, 1990; Li and Liao, 1993), this constraint on κ_H is released to prevent the computed stress from exceeding the maximum strength τ_0 of the material. Bonilla (2000) generalized the Masing rules further by defining a variable hysteresis scale factor κ_H which assures that the stress-strain path during each loading/reloading is bounded by the maximum shear strength τ_0. This hysteresis formulation was named the Generalized Masing rules because it includes the Cundall-Pyke hypothesis (Pyke, 1979) and Masing's original formulation as special cases.

In the hyperbolic model the damping ratio approaches $2/\pi$ ($\sim$64%) at large strains (Ishihara, 1996), which is much larger than the damping ratio of 25–40% observed in experimental data. Ishihara *et al.* (1985) suggested a method to control the damping ratio by computing a new backbone curve, which follows a hysteresis path controlled by the required damping ratio. The required strain-dependent damping ratio ξ_H is calculated with the following expression (Hardin and Drnevich, 1972):

$$\xi_H = \frac{\frac{\gamma_{xy}}{\gamma_r}}{1 + \left|\frac{\gamma_{xy}}{\gamma_r}\right|} \xi_{\max}, \tag{18}$$

where γ_{xy} is the level of deformation and $\xi_{\max}$ is the maximum damping ratio at large strains. By equating ξ_H in eq. 18 with the damping ratio from the hyperbolic model, NOAH finds a solution for the reference strain γ_r' that is compatible with the desired damping value ξ_H. This new reference strain γ_r' is then used to recompute the backbone curve, and the procedure is repeated for each time step. In addition to hysteretic damping, NOAH models intrinsic attenuation with constant Q by the rheology of the generalized Maxwell body (Day, 1998). For a more detailed description of the model refer to Bonilla (2001).

In the original NOAHH code, the maximum shear stress τ_0 for the backbone curve (eq. 16) is calculated from the angle of internal friction φ and cohesion c (Hartzell *et al.*, 2004) using the Mohr-Coulomb failure criterion (e.g. Jaeger *et al.*, 2007):

$$\begin{aligned} \tau_0 &= \sigma_m \cdot \sin(\varphi) + c \cdot \cos(\varphi) \\ \sigma_m &= \sigma_v \frac{1 + 2K_0}{3}, \end{aligned} \tag{19}$$

where σ_m is the effective mean stress, σ_v the vertical effective stress and K_0 the coefficient of Earth at rest. For the nonlinear simulations in the SLB, we prefer not to use this method, as we have little information about the parameters c and φ. Instead, we modified the code to require γ_r instead of c as the soil parameter and calculate τ_0 directly from γ_r using equation 15 (L.F. Bonilla, personal comm., 2009). Therefore, we need two nonlinear parameters for each layer: the reference strain γ_r and the maximum damping ratio $\xi_{\max}$.

Soil parameters

We extract the P-wave velocity v_p, the low-strain S-wave velocity v_s and the density ρ from the Wasatch Front Community Velocity Model (WFCVM Magistrale *et al.*, 2009), which is the model used for the LF FD simulations. For each site along the three profiles we extract v_p, v_s and ρ at a vertical spacing of 1 m (without constraining the velocities to a minimum value, as is often necessary for FD simulations due to computational limitations). The quality factors Q_p and Q_s are computed from v_s (in km s^{-1}) using an empirical relation derived by Brocher (2006):

$$\begin{aligned} Q_s &= \begin{cases} 13 & v_s < 0.3 \text{kms}^{-1} \\ -16 + 104.13\ v_s - 25.22\ v_s^2 + 8.21\ v_s^3 & v_s \geq 0.3 \text{kms}^{-1} \end{cases} \\ Q_p &= 2\ Q_s. \end{aligned} \tag{20}$$

Bay and Sasanakul (2005) performed resonant column and torsional shear tests on Bonneville clay soil samples collected at four different sites around the Wasatch front. The only sampling location that is within our computational domain is the BYU research site NW of SLC International airport (labeled "soil samples" in Fig. 10). Bay and Sasanakul (2005) concluded that the Bonneville soils exhibit more linear behavior, i.e. a smaller modulus reduction

and less damping, than would be predicted by commonly used empirical relationships (e.g. Vucetic and Dobry, 1991; Darendeli, 2001). To correct for this increased linearity they propose using a modified plasticity index (PI), which is 10% higher than the actual PI, for the relation of Vucetic and Dobry (1991). For the relationship of Darendeli (2001), Bay and Sasanakul suggest using a modified plasticity index PI', predicted with the following linear relation:

$$\mathrm{PI}' = 1.8956 \cdot \mathrm{PI} + 25.92 \tag{21}$$

For example, a PI of 2% was measured on the sample SLC35, extracted near SLC airport at 10.7 m depth. However, the best match between the observed and predicted modulus reduction and damping curves was obtained when using PI'=30% in Darendeli's relationship. We follow these recommendations and use the empirical relationships of Darendeli (2001) to predict γ_r and $\xi_{\max}$ from PI' and other parameters.

To assign a value for the modified plasticity index PI' to each site along the three profiles we use the Quaternary site response units (SRU, Fig. 10) mapped by McDonald and Ashland (2008). Table 2 summarizes the properties of the different SRUs and the values of PI' assigned to them. The clay rich composition of unit Q01 is reflected in the rather high PI' of 40%. Q02 has more silt, so a lower value of 30% was used for PI'. The lacustrine and alluvial deposits on the footwall of the Wasatch fault consist mostly of gravel and sand with little clay content. Thus, PI'=0% was used for SRU Q03. (James Bay, personal comm., 2009). Sites outside the basin which are classified as Tertiary (T), Mesozoic (M), Paleozoic or Precambrian (P) bedrock are treated as fully linear. We assumed a normal overconsolidation ratio (OCR of 1) for all units. Additionally NOAH requires the coefficient of Earth at rest K_0; here, we used K_0=0.5 for normal consolidation.

Darendeli (2001) proposed the following relation to predict the reference strain as a function of OCR, plasticity index (PI') and confining pressure σ_0:

$$\gamma_r = (\phi_1 + \phi_2 \cdot \mathrm{PI} \cdot \mathrm{OCR}^{\phi_3}) \cdot \sigma_0^{\phi_4} \tag{22}$$

The constants ϕ_1, ϕ_2, ϕ_3 and ϕ_4 are given in Darendeli (2001, Table 8.12). We determined the reference strain at 1 m depth intervals, assuming an average depth to the ground water table of 3 m to calculate σ_0. Additionally we evaluated the modulus reduction curve and its standard deviation σ using Darendeli's equations. By adding or subtracting σ from these modulus reduction curves and determining the strain where G/G_0=0.5, we defined an upper and lower value for the reference strain, $\gamma_r \pm \sigma$. We also computed the damping curve at each depth interval of 1 m and used the maximum to define the parameter $\xi_{\max}$. The equations for the damping curves are given in Darendeli (2001), and they require a frequency f and the number of cycles N; we used f=1 Hz and N=10. We also took the standard deviation of the damping ratio into account and determined $\xi_{\max} \pm \sigma_d$. The maximum damping ratios we obtained with this method vary between ∼25% near the surface and ∼20% at depth, with a standard deviation of 3-4%.

Figure 12 shows γ_r increasing with depth for a typical location on site response unit Q01 (site 100 along P_1). The R_1 interface at this site is located at ∼210 m depth, and it is accompanied by a sharp velocity contrast, with v_s increasing from 500 to 914 m·s^{-1}. We defined layers with a shear-wave velocity below 750 m·s^{-1} as nonlinear and the remaining layers as linear. The reference strain was formally set to 1% for the linear part of the structure in Fig. 12, even though γ_r is only used for nonlinear layers in NOAH.

The symbols in Figure 12 show the reference strain determined from the Bonneville clay soil samples at different confining pressures. Because the reference strain determined from the soil samples shows so much variability with the sampling location, we generate two additional

nonlinear models for each site, representing the upper and lower bound on nonlinearity. The lower bound nonlinear model is obtained by using $\gamma_r + \sigma$ for the reference strain and $\xi_{\max} - \sigma_d$ for the maximum damping ratio. Conversely, the upper bound nonlinear model uses $\gamma_r - \sigma$ and $\xi_{\max} + \sigma_d$ for the reference strain and maximum damping ratio, respectively. The dashed lines in Figure 12 show the $\gamma_r \pm \sigma$ as a function of depth. We perform nonlinear simulations with all three models to estimate the sensitivity of the final ground motion to uncertainties in the soil parameters.

Finite difference parameters

Since the shear-wave velocity may decrease during strong shaking due to nonlinearity, simulations of such effects require a finer spatial discretization than linear simulations. NOAH comes with a helper program that computes the required spatial step Δx and temporal discretization Δt to meet the stability criterion:

$$\Delta x = \frac{v_{s,\min}}{f_{\max}\ n}$$
$$\Delta t = p_0 \frac{\Delta x}{v_{s,\max}},$$

where p_0 is the Courant number, n is the number of grid points per wavelength and $f_{\max}$ is the maximum simulated frequency. We used n=30 and p_0=0.5 to ensure numerical stability and selected $f_{\max}$=20 Hz to cover a broad frequency range for the BB simulations. Because the minimum and maximum shear-wave velocity vary with the local geology, different values for the spatial and temporal discretization are used for each site along the three profiles. We simulated 60 seconds of nonlinear wave propagation, using the entire length of synthetics available from the FD and BB simulations.

Boundary conditions and input signals for nonlinear simulations

We apply a deconvolution to the surface BB synthetics to obtain a signal that represents the wavefield at 240 m depth, where the base of the soil column used for the 1-D nonlinear simulations is located. For the deconvolution we use the top 240 m in the velocity model that was employed for the 3-D LF simulations. Because the latter differs from the 1-D nonlinear model in resolution and minimum v_s, we also perform a 1-D linear simulation for each site along the two profiles in order to ascertain how much of the difference between linear and non-linear synthetics is related to nonlinearity in the soil model.

NOAH provides two different options for the boundary conditions (BC) at the base of the soil layer: rigid and elastic. Many numerical studies on nonlinear soil behavior use borehole records as input signals (e.g. Bonilla *et al.*, 2005). As it is often not possible to separate the upgoing from the downward reflected wavefield, downhole records are used in combination with rigid BCs. In this case the motion at the base of the column is prescribed by the borehole signal at any time. This approximation allows no energy to be radiated back into the underlying medium, and may produce multiple reflections within the soil column (Joyner and Chen, 1975). These resonances are naturally avoided if the dissipation within the soil column is large enough, especially in the case of strong nonlinearity.

We tested this approach by deconvolving the BB signal at site P1-100 for borehole conditions using a detailed 1-D model of the top 240 m, and propagating this signal back to the surface using NOAH in linear mode (Fig. 13 top). The resulting ground motion should be identical to the the original BB under ideal conditions. However, the spectra of the resulting

surface acceleration exhibits some strong peaks which were not present in the original BB spectra, with the first peak located near 0.5 Hz. This frequency is very close to the expected resonance frequency of the soil column, which is ∼0.57 Hz with an average shear-wave velocity of 547 m·s^{-1} and 240 m thickness (dashed line in Fig. 13). Therefore, rigid BCs are not suitable for this study, since we must expect that dissipation will be low at some sites due to low nonlinearity.

Instead, we decided to use the elastic BCs described by Joyner and Chen (1975) at the base of the soil column. These transmitting BCs allow propagation of waves into the underlying medium, but they require the incident wavefield as input signal. We computed the transfer function between the free surface and a model with the top 240 meters removed and used it to deconvolve the free-surface BB synthetics. As the resulting signals represent outcrop records, their amplitude was divided by two to obtain the incoming wavefield at depth. We verified this method by propagating this signal back to the surface using NOAH with elastic BCs. The signal obtained after the deconvolution and 1-D propagation (Fig. 13 bottom) is very similar to the original BB input in the time and frequency domains. For this reason we chose transmitting BCs in NOAH, and applied the procedure described above to find the incoming wavefield at depth.

Linear broadband synthetics

Figure 14 shows LF and linear BB synthetic velocity records from scenario earthquake B' in the time and frequency domains at three selected sites . The Fourier spectra of the LF synthetics exhibit a sharp drop-off at frequencies above 1 Hz while the BB synthetics contain energy up to 20 Hz, with a matching frequency of 0.9±0.1 Hz. The seismograms at sites 2287 (SLC international airport) and 2289 (downtown SLC) are dominated by the surface waves present in the LF synthetics, which generate horizontal peak ground velocities up to 1.27 m·s^{-1} in the E-W direction at site 2287 and up to 1.78 m·s^{-1} in the N-S direction at site 2289. The surface waves are less pronounced at the site BSS, and consequently the HF component contributed by the scatterograms is more evident.

The broadband frequency content of these synthetics allows us to compute spectral accelerations (SAs) at frequencies above 1 Hz. As with the low-frequency synthetics, we compute the geometric mean of both horizontal components using the orientation-independent GMRotD50 measure (Boore *et al.*, 2006).

Figure 15 compares BB SAs as function of distance along two cross-sections with SAs predicted by the same four next-generation ground motion prediction equations (GMPEs) used previously: Boore and Atkinson (2008), Campbell and Bozorgnia (2008), Abrahamson and Silva (2008) and Chiou and Youngs (2008) (BA08, CB08, AS08 and CY08, respectively). For each site along the three cross-sections, we used the 3-D fault model and 3-D velocity mesh to calculate the rupture distance R_{Rup}, the horizontal distance to both the top of the rupture, R_x, and to the surface projection of the rupture, R_{JB}, the average shear-wave velocity in the top 30 meters V_{S30}, and other site-specific parameters required by the GMPEs.

Figure 15 (left) shows BB 0.2s-SAs along cross-section P0 for rupture model B. The highest accelerations are encountered on the hanging-wall close to the fault, where the SAs predicted by all four GMPEs are exceeded for $R_x < 5$ km. The GMPE by BA08, which predicts the lowest amplitudes of the four considered relations, yields 0.2s-SAs that are two to four times lower than the BB 0.2s-SAs in this area. Even the relations of CY08 and AS08, which predict the highest amplitudes, are exceeded at near-fault hanging-wall locations. On the footwall side of the fault, the BB SAs are in good agreement with BA08. Beyond fault distances of more

than 12 km on the hanging-wall side, however, the BB SAs quickly drop below the values predicted by all four NGA models. The simulated SAs are generally within one standard deviation of those predicted by the NGA relations everywhere along the cross-section.

Figure 15 (right) shows BB 0.2s-SAs along cross-section P1 for rupture model B'. This example includes the most extreme values produced by our simulations, as rupture model B' yields the largest ground motions of all six scenarios and the cross-section P1 runs through the area with the largest linear BB SAs for this scenario. For fault distances less than 9 km on the hanging-wall side, the linear BB SAs exceed the predictions of all four considered NGA models by more than one standard deviation. All four GMPEs predict the highest SAs on the footwall side of the fault, which is the opposite of the pattern produced by the BB simulations. However, the BB results presented in Figures 14–15 do not take soil nonlinearity into account by any means, the subject of the following section.

Nonlinear 1-D simulations

To estimate the impact of nonlinear soil behavior at frequencies above 1 Hz, we carried out fully nonlinear 1-D simulations for each site along the three profiles using the methodology previously described. Figure 16 shows an example of 1-D nonlinear simulation for site 100 along profile 1 (P1-100), located 5.3 km west of the fault trace (Fig. 10). The linear BB signal shows spikes with peak accelerations up to 9 $\mathrm{m{\cdot}s^{-2}}$ (Fig. 16 a). This signal is deconvolved to represent the incoming wavefield at depth, and propagated back to the surface using NOAH. The resulting signal on the surface of the nonlinear layer exhibits lower peak ground accelerations of up to 3 $\mathrm{m{\cdot}s^{-2}}$.

Spectral accelerations of the nonlinear signal (Fig. 16 b) are generally much lower at frequencies above 1 Hz. The original BB signal shows two peaks at 1.6 and 3.7 Hz, with spectral amplitudes of 29 and 29.5 $\mathrm{m{\cdot}s^{-2}}$, respectively. Nonlinear site response reduces the amplitudes of the two peaks to 17 and 16 $\mathrm{m{\cdot}s^{-2}}$, respectively, and their frequencies are slightly reduced to 1.4 and 2.7 Hz, respectively. This shift of resonance frequencies to lower values is caused by shear modulus degradation due to nonlinear behavior of the soil.

At this site, the soil is allowed to behave nonlinearly in the top 210 meters. However, the peak shear strain remains below the reference strain for depths larger than 90 m (Fig. 16 c). At depths between 5 and 90 meters, the peak shear strain exceeds the reference strain, which indicates that the soil exhibits strong nonlinear behavior. The maximum shear strain and acceleration (Fig. 16 d) peak at a depth of 70 meters. This peak is probably linked to the local minimum in the shear-wave velocity profile at the same depth (Fig. 16 e), which may be trapping the seismic waves. The stress-strain relation (Fig. 16 f) is close to linear 100 m below the surface, but becomes increasingly hysteretic with decreasing depth.

Figure 17 shows SAs predicted by the four NGA models for the same profiles as depicted in Figure 15, but compares them with spectral accelerations calculated from the fully nonlinear synthetics (NL SAs). For cross-section P0 and rupture model B (Fig. 17 left), the NL 0.2s-SAs are generally consistent with the values predicted by AS08 and CY08 at near-fault ($R_x < 10$ km) hanging-wall locations. Spectral accelerations predicted by BA08 and CB08, however, are up to 50% lower than NL 0.2s-SAs in the hanging wall. Compared to the BB 0.2s-SAs, the NL 0.2s-SAs are reduced by up to 45%. On the footwall side and for $R_x > 15$ km on the hanging-wall side, the NL 0.2s-SAs are almost identical with BB 0.2s-SAs. This observation suggests that the input ground motion at these sites is not sufficient to trigger nonlinear soil response.

We also calculated the site response at every point along the three profiles using the soil

models that represent the upper and lower bound of soil nonlinearity, by taking $\gamma_r \mp \sigma$ as the reference strain and $\xi_{\max} \pm \sigma_r$ as maximum damping ratio. The hatched area in Figure 17 (left) indicates the range of NL 0.2s-SAs obtained from the upper and lower bound parameters. The choice of γ_r and $\xi_{\max}$ only affects the ground motion at sites where a significant deamplification due to soil nonlinearity takes place; that is, on the hanging wall site of the fault for R_x less than about 10 km. Using the lower bound soil model increases NL 0.2s-SAs by up to 30% at individual sites, while the upper bound model decreases them by up to 25% compared to the reference nonlinear model.

Figure 17 (right) makes the same comparison with NL 0.2s-SAs for cross-section P1 and rupture model B'. Compared to the linear case, 0.2s-NL SAs are reduced by up to 70%, with the largest reduction on the hanging-wall side within 10 km fault distance. The simulated 0.2s-SAs are in general agreement with the GMPEs. Even when the uncertainty associated with the nonlinear soil parameters is taken into account (hatched area in Fig. 17, right), the NL 0.2s-SAs remain mostly inside one standard deviation of the minimum and maximum of the four considered NGA predictions. The largest NL 0.2s-SAs along cross-section P1 occur close to the surface rupture on the footwall side, which is consistent with the pattern predicted by the four GMPEs. Along cross-section P1, all locations on the hanging-wall side belong to site response unit Q01 (Fig. 10), while the footwall side is located on unit Q03 and on rock. This fact suggests that the degree of nonlinearity is controlled by the local site response unit.

Discussion

Low-frequency simulations

Figure 18 shows average spectral acceleration ratios (SARs) as a function of horizontal distance from the top of the rupture, R_x, along two cross-sections oriented perpendicular to the fault (Fig. 8). We computed the SARs by dividing the spectral acceleration along the cross-section by the value obtained on a reference site on the footwall. SARs are shown for five different frequencies from 0.2 to 1.0 Hz. Along cross-section 1 the SARs peak near 2.5 km from the surface rupture for 0.2 Hz, but peak between 1.0 and 2.5 km distance for other frequencies. The SARs along cross-section 2 peak between 1 and 5 km distance from the surface rupture, with the maximum SARs occurring closer to the fault for shorter wavelengths. This wavelength-dependent amplification pattern is consistent with the basin-edge effect, which is caused by interference between edge-generated surface waves and the direct S-wave (e.g. Kawase, 1996; Pitarka *et al.*, 1998). Surface wave dispersion results in longer wavelengths traveling faster than shorter wavelengths, shifting the location of interference with the direct S-wave further away from the fault. Hallier *et al.* (2008), for example, performed 2D simulations for a basin bounded by a 68°-dipping normal fault and observed that the maximum amplification occurs further away from the fault for the low-frequency band (0-2 Hz) than for the high-frequency band (2-4Hz). Figure 18 suggests that the peaks in 2s-SAs and 3s-SAs between 1 and 5 km from the surface rupture and their drop-off near the rupture can be explained by the basin-edge effect.

The approximation of velocity strengthening in the dynamic rupture models provides an alternative explanation for the occurrence of peak SAs at a distance from the fault. As a consequence of forcing $\mu_d > \mu_s$ near the free surface, peak slip rates tend to be lower in the uppermost 4 km of the fault than at greater depth (Fig. 4). Therefore, the possibility cannot be excluded that the drop-off in simulated SAs near the fault is caused, at least in part, by the emulated velocity strengthening.

Aagaard *et al.* (2004) studied rupture directivity effects for strike-slip earthquakes on vertical faults and for thrust earthquakes on shallow dipping faults. They concluded that strong directivity effects exist only if the rupture propagates parallel to the direction of the fault slip vector. In the case of dip-slip rupture, this conclusion implies that a moderate directivity effect exists in the up-dip direction for deep hypocenters, while directivity effects are minimal in the along-strike direction for unilateral ruptures. The along-strike rupture direction effects that are obvious from the differences between scenarios A and A' and between scenarios B and B' seem to contradict the findings of Aagaard *et al.* (2004). However, the wave propagation simulations presented in this paper were performed for a velocity mesh with strong lateral heterogeneities, while the material properties varied only with depth in the simulations of Aagaard *et al.* (2004). It is obvious that Love and Rayleigh waves generated at the lateral discontinuity between the hanging wall and the footwall side of the surface rupture contribute to the strong ground motion on the low-velocity sediments of the SLB. As the rupture propagates in the along-strike direction these surface waves are continuously generated at the basin-edge, interfering with each other to generate a directivity pattern. The absence of lateral material heterogeneities near the free surface may explain why Aagaard *et al.* (2004) did not report a strong directivity effect in the along-strike direction for the thrust fault.

Broadband simulations

Published hybrid BB generation methods differ in the details of merging the LF and HF portions of the synthetics, as well as in the dependency of the HF part on the local impedance structure. For example, the method by Graves and Pitarka (2010) incorporates effects of the velocity structure into the HF part of the spectrum, which is otherwise independent of the LF spectral level. On the other hand, the HF scatterograms computed by the method of Mai *et al.* (2010) are scaled with the amplitude of the LF spectra at the matching frequency (0.9±0.1 Hz), in part to minimize numerical artifacts at the merging frequency for the LF and HF portions, but also to transfer impedance effects from the LFs into the HFs. This dependency between the amplitude of the LF and HF components in the BB synthetics causes, to some extent, the distributions of SAs at higher frequencies to resemble those for longer periods. Maps with SAs predicted by GMPEs generally exhibit a different spatial distribution depending on the analyzed frequency as noted in the previous section. Future validation exercises for normal-faulting events should focus on resolving this issue.

The assumptions involved in simulating nonlinear soil behavior represent some limitations to this study. A first source of uncertainty concerns the nonlinear soil parameters γ_r and $\xi_{\max}$. While the empirical relations we used to estimate these parameters were modified based on laboratory tests of Bonneville clay samples, only one of the sampling locations was inside the area considered for this study. No laboratory measurements were performed on soil samples representing SRU Q02 and Q03, so the lower reference strain assigned to these units is based solely on the relationship by Darendeli (2001). To analyze the sensitivity of our results to parameter selection we included soil models that represent 1σ limits of soil nonlinearity. Results obtained with the lower bound nonlinear model (Fig. 17) suggest that nonlinearity has a significant impact at near-fault hanging-wall sites even for a more conservative choice of reference strain.

The simplicity of the soil model, which neglects dilatancy, constitutes a further limitation. Observations of spiky waveforms, e.g. during the 1987 Superstition Hills (Holzer *et al.*, 1989; Zeghal and Elgamal, 1994), the 1995 Hyoge-ken Nanbu (Kamae *et al.*, 1998) and the 1993

Kushiro-Oki earthquake (Iai *et al.*, 1995) support the idea that soft soils partly recover their shear strength under cyclic loads due to their dilatant nature (Bonilla *et al.*, 2005). During this short recovery phase the soil regains its capability to transmit the incoming seismic energy to the surface, leading to characteristic cusped waveforms that represent large amplifications. Modeling dilatancy with NOAH requires 5 additional parameters, which need to be calibrated from stress-controlled laboratory experiments (e.g. Iai *et al.*, 1990a; Bonilla, 2001; Roten *et al.*, 2009). To our knowledge, no such measurements have been performed on soil samples from the Salt Lake region, which led us to ignore dilatancy in our nonlinear simulations. Including dilatancy may result in higher spectral accelerations especially on the hanging-wall side.

Finally, the assumption that the site response is adequately represented by a 1-D model is likely to represent the largest limitation. In geotechnical engineering it is generally accepted that the major part of ground shaking is related to upward propagation of body waves (e.g. Ishihara, 1996). This assumption is often justified with the bending of seismic rays towards the Earth's surface, since seismic velocities increase with depth in a typical geological setting. However, Bard and Bouchon demonstrated in 1980a that Love waves generated at a basin edge may have much larger amplitudes than the direct incident signal even in the case of vertical incidence. Such basin-diffracted waves have been identified in many weak motion records (e.g. Field, 1996; Hartzell *et al.*, 2003; Roten *et al.*, 2008). The physics of surface wave propagation in nonlinear media is an ongoing field of research, and numerical codes are under development that will allow the treatment of wave propagation in nonlinear materials in two (e.g. Bonilla *et al.*, 2006) or three dimensions (e.g. Taborda and Bielak, 2008) in the future.

Conclusions

We performed numerical simulations for six M 7 scenario earthquakes on the WFSLC with the finite difference method for frequencies up to 1 Hz. These six scenarios are based on four rupture models obtained from simulations of spontaneous rupture on a planar, vertical normal fault with depth-dependent normal stress. We assess our results using horizontal spectral accelerations at 3s and 2s computed from the simulated ground motions. Significant along-strike rupture direction effects occur for events nucleating near either end of the segment. Events A' and B', which nucleate near the southern end, generate much larger ground motions (2s-SAs of up to 1.4 g) in the downtown SLC area than events A and B, which initiate near the northern end (2s-SAs < 0.5 g). The fact that identical rupture models generate such different ground motion patterns when mirrored laterally is probably the result of a combination of source directivity and site effects. These results are especially significant since the southern barrier was identified as the most likely initiation point during past earthquakes (Bruhn *et al.*, 1992). Events C and D, which nucleate near the central barrier, generate intermediate ground motions (2s-SAs up to $\sim$1 g) north of SLC and up to 0.6 g in the downtown SLC area. Results from these two scenarios suggest that a rupture direction effect is also present along the dip direction, with the deeper hypocenter generating larger ground motions than the shallower hypocenter.

Average SAs from the six scenarios reach or exceed 0.3 g at 3 seconds and 0.6 g at 2 seconds on the deep sediments west of the Warm Springs section, near downtown SLC and near the Cottonwood Heights area. We find that the simulated ground motions are generally consistent with four recent NGA relations. Average spectral accelerations on the hanging wall exceed the prediction of BA08 by $\sim$25% for 3s-SAs and $\sim$40% for 2s-SAs where $R_{\mathrm{JB}} \leq 1$ km, but they are consistent with predictions by CB08, AS08 and CY08 for R_JB=0 and $R_{\mathrm{Rup}} < 4$ km.

We apply the hybrid BB method of Mai *et al.* (2010), including a finite-fault approximation developed by Mena *et al.* (2010), to add a high-frequency (1–10 Hz) component to the LF (0–10 Hz) FD synthetics produced for an M 7.0 earthquake on the WFSLC. Comparisons to the ground motions predicted by four recent NGA relations show that 0.1s- and 0.2s-SAs derived from the linear BB synthetics often exceed empirical SA estimates by more than one standard deviation at near-fault hanging-wall locations. Because SAs at 2s and 3s agree well with empirical values, we infer that the mismatch at higher frequencies is caused by nonlinear soil behavior, which was neglected in the BB generation methodology.

Using the nonlinear 1-D propagator NOAH we calculate the site response in a yielding soil at 454 sites arranged along three E-W cross-sections. The input signal for these simulations is obtained by deconvolving BB synthetics at the free surface to a subsurface location at 240 m depth under the assumption of vertical incidence. We use a simple soil model that only requires the reference strain γ_r and maximum damping ratio $\xi_{\max}$ as additional parameters, which we estimate from empirical relationships (Darendeli, 2001) that were modified based on laboratory tests on Bonneville clay samples (Bay and Sasanakul, 2005). SAs of the resulting nonlinear 0–10 Hz synthetics are in agreement with GMPE predictions within approximately 1σ, including sites at near-fault hanging-wall locations.

0.2s-SAs and 0.1s-SAs corrected for nonlinear soil behavior compare favorably with values predicted by four GMPEs, including areas at close distances (< 5 km) from the rupture. Further comparisons against strong motion data are required to validate the simulated ground motions.

Data and resources

The Wasatch Front Community Velocity Model (WFCVM) is available from the Utah Geological Survey (`http://geology.utah.gov/ghp/consultants/geophysical_data/cvm.htm`, last accessed May 2011). Maps presented in this text were made using the Generic Mapping Tools version 4.5.0 (`http://www.soest. hawaii.edu/gmt`, last accessed May 2011) by Wessel and Smith (1998). 3D graphics and animations were created with the Visualization toolkit (`http://www.vtk.org`, last accessed May 2011) by Schroeder *et al.* (2006). 2D plots were created with the Matplotlib (`http://matplotlib.sourceforge.net`, last accessed May 2011) graphics package for Python (Hunter, 2007). We used the OPENSHA attenuation relationship plotter (`http://www.opensha.org`, last accessed May 2011) and the MatLab^{TM}scripts from the Baker research group (`http://www.stanford.edu/~bakerjw /attenuation.html`, last accessed May 2011) to generate attenuation curves. The nonlinear 1-D code NOAH (Bonilla *et al.*, 2005) and the BB toolbox (Mai *et al.*, 2010; Mena *et al.*, 2010) are available from their authors upon request.

Simulations of wave propagation and spontaneous rupture were performed on the Teragrid resources NICS (National Institute for Computational Sciences) Kraken and TACC (Texas Advanced Computing Center) Ranger under an NSF allocation. The generation of the kinematic source from the spontaneous rupture results requires considerable amount of computational time due to the spatial and temporal interpolations and the volume of the data. We implemented the moment-rate generation code as a parallel application using the `MPI-2` library, reducing the wall-clock time to less than 3 hours per scenario using 36 cores on NICS Kraken. This tool directly generates source partitions suitable for parallel I/O in the wave propagation code.

Tables

Table 1: Key parameters in FD simulations of wave propagation.

Model dimensions	1500 × 1125 × 750 ($1.3{\cdot}10^9$ nodes) 60 (N-S) × 45 (E-W) × 30 (vertical) km
Simulation length	60 s (24,000 time steps)
Horizontal discretization Δh	40 m
Temporal discretization Δt	$2.5{\cdot}10^{-3}$ s
Minimum v_s	200 m·s^{-1}
Highest frequency	1.0 Hz
Number of CPU cores	1875
Wall-clock runtime	2.5 hrs (NICS Kraken)

Table 2: Site response units, Plasticity Index (PI') and average V_{S30}.

Unit(s)	Description (McDonald and Ashland, 2008)	PI'	$\overline{V_{S30}}$ (m·s^{-1})
Q01	Lacustrine and alluvial silt, clay and fine sand; alluvial, lateral-spread, or marsh deposits typically overlie lacustrine deposits	40%	250
Q02	Lacustrine sand and gravel; interbedded lacustrine silt, clay and sand; latest Pleistocene to Holocene alluvial fan deposits	30%	375
Q03	Lacustrine and alluvial gravel and sand; pre-Bonneville alluvial fan deposits, primarily where they occur on the footwall of the Wasatch fault	0%	507
T,M,P	Tertiary, mesozoic, paleozoic or precambrian rock; treated as linear.		

Acknowledgements

This research was supported by the U.S. Geological Survey, Department of the Interior, under USGS award numbers 06HQGR0205 and 06HQGR0206, and by a fellowship for prospective researchers (to Daniel Roten) from the Swiss National Science Foundation (PBEZ22-117264). The views and conclusions contained in this document are those of the authors and should not be interpreted as necessarily representing the official policies, either expressed or implied, of the U.S. Government.

References

Aagaard, B.T., Hall, J.F., and Heaton, T.H. 2004. Effects of Fault Dip and Slip Rake Angles on Near-Source Ground Motions: Why Rupture Directivity Was Minimal in the 1999 Chi-Chi, Taiwan, Earthquake. *Bull. seism. Soc. Am.*, 155–170.

Abrahamson, N., and Silva, W. 2008. Summary of the Abrahamson & Silva NGA ground-motion relations. *Earthquake Spectra*, **24**(1), 67–97.

Adan, S.M., and Rollins, K.M. 1993. *Damage potential index mapping for Salt Lake Valley, Utah.* Misc. Pub 93-4. Utah Geol. Surv.

Andrews, DJ. 1976. Rupture propagation with finite stress in antiplane strain. *J. Geophys. Res*, **81**(20), 3575–3582.

Bard, P.-Y., and Bouchon, M. 1980a. The seismic response of sediment-filled valleys. Part 1. The case of incident SH waves. *Bull. seism. Soc. Am.*, **70**(4), 1263–1286.

Bard, P.-Y., and Bouchon, M. 1980b. The seismic response of sediment-filled valleys. Part 2. The case of incident P and SV waves. *Bull. seism. Soc. Am.*, **70**(5), 1921–1941.

Bay, J.A., and Sasanakul, I. 2005. *Measurement of nonlinear dynamic properties of Bonneville silty-clays.* Award 04HQGR0055. Utah State Univ., Department of Civil and Environmental Engineering.

Benz, H.M., and Smith, R.B. 1988. Elastic-wave propagation and site amplification in the Salt Lake valley, Utah, from simulated normal faulting earthquakes. *Bull. Seism. Soc. Am.*, **78**(6), 1851–1874.

Black, B.D., Lund, W.R., and Mayes, B.H. 1995. Large earthquakes on the Salt Lake City segment of the Wasatch fault zone-summary of new information from the South Fork Dry Creek site, Salt Lake County, Utah. *Pages 11–30 of: Environmental and Engineering Geology of the Wasatch Front Region: 1995 Symposium and Field Conference. W.R. Lund(Editor).* Utah Geological Association Publication 24.

Bonilla, L.F. 2000. *Computation of linear and nonlinear site response for near field ground motion.* Ph.D. thesis, University of California, Santa Barbara.

Bonilla, LF. 2001. NOAH: Users Manual. *Institute for Crustal Studies, University of California, Santa Barbara.*

Bonilla, LF, Lavallee, D., and Archuleta, RJ. 1998. Nonlinear site response: Laboratory modeling as a constraint for modeling accelerograms. *The Effects of Surface Geology on Seismic Motion*, **2**, 793–800.

Bonilla, L.F., Archuleta, R.J., and Lavallee, D. 2005. Hysteretic and Dilatant Behavior of Cohesionless Soils and Their Effects on Nonlinear Site Response: Field Data Observations and Modeling. *Bull. Seism. Soc. Am.*, **95**(6), 2373–2395.

Bonilla, L.F., Luis, P.-C., and Nielsen, S. 2006. 1D and 2D linear and nonlinear site response in the Grenoble area. *In: Third International Symposium on the Effects of Surface Geology on Seismic Motion, Grenoble, France, 30 August - 1 September 2006.*

Boore, D. M., and Atkinson, G. M. 2008. Ground-Motion Prediction Equations for the Average Horizontal Component of PGA, PGV, and 5%-Damped PSA at Spectral Periods between 0.01 s and 10.0 s. *Earthquake Spectra*, **24**(1), 99–138.

Boore, D.M., Watson-Lamprey, J., and Abrahamson, N.A. 2006. Orientation-Independent Measures of Ground Motion. *Bull. Seism. Soc. Am.*, **96**(4A), 1502–1511.

Borcherdt, R.D. 1994. Estimates of site-dependent response spectra for design (methodology and justification). *Earthq. Spectra*, **10**, 617653.

Brocher, T. 2006. Key Elements of Regional Seismic Velocity Models for Ground motion simulations. *In: Proc. of Int. Workshop on Long-Period Ground Motion simulations and velocity structures, Tokyo, Nov 14-15, 2006.*

Bruhn, R.L., Gibler, P.R., Houghton, W., and Parry, W.T. 1992. Structure of the Salt Lake segment, Wasatch normal fault zone: Implications for rupture propagation during normal faulting. *In: Assessment of Regional Earthquake Hazards and Risk Along the Wasatch Front, Utah.* U.S. Geol. Surv. Prof. Pap.,1500-A-J, H1–H25.

Campbell, K. W., and Bozorgnia, Y. 2008. NGA Ground Motion Model for the Geometric Mean Horizontal Component of PGA, PGV, PGD and 5% Damped Linear Elastic Response Spectra for Periods Ranging from 0.01 to 10 s. *Earthquake Spectra*, **24**(1), 139–171.

Chiou, B., Darragh, R., Gregor, N., and Silva, W. 2008. NGA strong-motion database. *Earthquake Spectra*, **24**(1), 23–44.

Chiou, B.S.J., and Youngs, R.R. 2008. An NGA model for the average horizontal component of peak ground motion and response spectra. *Earthquake Spectra*, **24**(1), 173–215.

Cornou, C., Bard, P.-Y., and Dietrich, M. 2003. Contribution of Dense Array Analysis to the Identification and Quantification of Basin-Edge-Induced Waves, Part II: Application to Grenoble basin (French Alps). *Bull. Seism. Soc. Am.*, **93**, 2624–2648.

Cruz-Atienza, V.M., Olsen, K.B., and Dalguer, L.A. 2009. Estimation of the breakdown slip from strong-motion seismograms: insights from numerical experiments. *Bull. seism. Soc. Am.*, **99**(6), 3454.

Cui, Y., Olsen, K.B., Lee, K., Zhou, J., Small, P., Roten, D., Ely, G., Panda, D.K., Chourasia, A, Levesque, J., Day, S.M., and Maechling, P. 2010. Scalable Earthquake Simulation on Petascale Supercomputers. *In: Proceedings of SC10, November 13-19, New Orleans, LA.*

Dalguer, L. A., and Mai, M. 2008. Implications of Style-of-Faulting and Loading Characteristics on the Dynamic Rupture Process. *AGU Fall Meeting Abstracts*, Dec., D1798+.

Dalguer, L.A., and Day, S.M. 2007. Staggered-grid split-node method for spontaneous rupture simulation. *J. Geoph. Res.*, **112**, B02302.

Dalguer, L.A., Miyake, H., Day, S.M., and Irikura, K. 2008. Surface rupturing and buried dynamic-rupture models calibrated with statistical observations of past earthquakes. *Bull. seism. Soc. Am.*, **98**(3), 1147.

Darendeli, Mehmet B. 2001. *Development of a new family of normalized modulus reduction and material damping curves.* Ph.D. thesis, The University of Texas at Austin.

Day, S.M. 1998. Efficient simulation of constant Q using coarse-grained memory variables. *Bull. seism. Soc. Am.*, **88**(4), 1051.

Day, S.M., and Bradley, C.R. 2001. Memory-efficient simulation of anelastic wave propagation. *Bulletin of the Seismological Society of America*, **91**(3), 520.

Day, S.M., and Ely, G.P. 2002. Effect of a shallow weak zone on fault rupture: numerical simulation of scale-model experiments. *Bull. seism. Soc. Am.*, **92**(8), 3022.

Dreger, D., Tinti, E., and Cirella, A. 2007. Slip velocity function parameterization for broad-band ground motion simulation. *Pages 11–13 of: Seismological Society of America 2007 Annual Meeting Waikoloa, Hawaii.*

Field, E. H. 1996. Spectral amplification in a sediment-filled valley exhibiting clear basin-edge-induced waves. *Bull. seism. Soc. Am.*, **86**, 991–1005.

Frankel, A., Carver, D., Cranswick, E., Bice, T., Sell, R., and Hanson, S. 2001. Observations of basin ground motion from a dense seismic array in San Jose, California. *Bull. seism. Soc. Am.*, **91**, 1–12.

Fukuyama, E., Mikumo, T., and Olsen, K.B. 2003. Estimation of the critical slip-weakening distance: Theoretical background. *Bull. seism. Soc. Am.*, **93**(4), 1835.

Graves, R.W., and Pitarka, A. 2010. Broadband Ground-Motion Simulation Using a Hybrid Approach. *Bull. seism. Soc. Am.*, **100**(5A), 2095.

Guatteri, M., Mai, P.M., Beroza, G.C., and Boatwright, J. 2003. Strong ground-motion prediction from stochastic-dynamic source models. *Bull. seism. Soc. Am.*, **93**(1), 301.

Hallier, S., Chaljub, E., Bouchon, M., and Sekiguchi, H. 2008. Revisiting the basin-edge effect at Kobe during the 1995 Hyogo-Ken Nanbu Earthquake. *Pure. Appl. Geophys.*, **165**, 1751–1760.

Hardin, BO, and Drnevich, VP. 1972. Shear modulus and damping in soils: design equations and curves. *ASCE Journal of Soil Mechanics & Foundations Div*, **98**(sm7), 667–692.

Hartzell, S., Carver, D., Williams, R. A., Harmsen, S., and Zerva, A. 2003. Site Response, Shallow Shear-Wave Velocity, and Wave Propagation at the San Jose, California, Dense Seismic Array. *Bull. seism. Soc. Am.*, **93**(1), 443–464.

Hartzell, S., Bonilla, L. F., and Williams, R.A. 2004. Prediction of Nonlinear Soil Effects. *Bull. Seism. Soc. Am.*, **94**(5), 1609–1629.

Hartzell, S., Guatteri, M., Mai, P.M., Liu, P.-C., and Fisk, M. 2005. Calculation of Broad-band Time Histories of Ground Motion, Part II: Kinematic and Dynamic Modeling Using Theoretical Green's Functions and Comparison with the 1994 Northridge Earthquake. *Bull. seism. Soc. Am.*, **95**(2), 614–645.

Hill, J., Benz, H., Murphy, M., and Schuster, G. 1990. Propagation and resonance of SH waves in the Salt Lake Valley, Utah. *Bull. Seism. Soc. Am.*, **80**(1), 23–42.

Holzer, T.L., Youd, T. L., and Hanks, T.C. 1989. Dynamics of Liquefaction during the 1987 Superstition Hills, California, Earthquake. *Science*, **244**(4900), 56–59.

Hunter, John D. 2007. Matplotlib: A 2D Graphics Environment. *Computing in Science and Engineering*, **9**, 90–95.

Iai, S., Matsunaga, Y., and Kameoka, T. 1990a. Parameter identification for a cyclic mobility model. *Report of the Port and Harbour Research Institute*, **29**, 57–83.

Iai, S., Matsunaga, Y., and Kameoka, T. 1990b. Strain space plasticity model for cyclic mobility. *Report of the Port and Harbour Research Institute*, **29**, 27–56.

Iai, S., Morita, T., Kameoka, T., Matsunaga, Y., and Abiko, K. 1995. Response of a dense sand deposit during 1993 Kushiro-Oki Earthquake. *Soils Found.*, **35**, 115–131.

Irikura, K., and Kamae, K. 1994. Estimation of strong ground motion in broad-frequency band based on a seismic source scaling model and an empirical Green's function technique. *Annals of Geophysics*, **37**(6).

Ishihara, K. 1996. *Soil Behaviour in Earthquake Geotechnics*. Clarenton Press, Oxford.

Ishihara, K., Yoshida, N., and Tsujino, S. 1985. Modelling of stress-strain relations of soils in cyclic loading. *Pages 373–380 of: International conference on numerical methods in geomechanics, Nagoya*.

Jaeger, J.C., Cook, N.G.W., Zimmerman, R.W., and Zimmerman, R.W. 2007. *Fundamentals of rock mechanics*. Wiley-Blackwell.

Joyner, W.B., and Chen, A.T.F. 1975. Calculation of nonlinear ground response in earthquakes. *Bull. seism. Soc. Am.*, **65**(5), 1315–1336.

Kamae, K., Irikura, K., and Pitarka, A. 1998. A technique for simulating strong ground motion using hybrid Green's function. *Bull. seism. Soc. Am.*, **88**(2), 357.

Kaneko, Y., Lapusta, N., and Ampuero, J.P. 2008. Spectral element modeling of spontaneous earthquake rupture on rate and state faults: Effect of velocity-strengthening friction at shallow depths. *J. Geophys. Res.*, **113**(B9), B09317.

Kawase, H. 1996. The Cause of the Damage Belt in Kobe: "The Basin-Edge Effect, "Constructive Interference of the Direct S-Wave with the Basin-Induced Diffracted/Rayleigh Waves. *Seism. Res. Lett.*, **67**(5), 25–34.

Konno, K., and Ohmachi, T. 1998. Ground-Motion Characteristics Estimated from Spectral Ratio between Horizontal and Vertical Components of Microtremor. *Bull. seism. Soc. Am.*, **88**(1), 228–241.

Li, X., and Liao, Z. 1993. Dynamic skeleton curve of soil stress-strain relation under irregular cyclic loading. *Earthq. Res. China*, **7**, 469–477.

Machette, M.N., Personius, S.F., Nelson, A.R., Schwartz, D.P., and Lund, W.R. 1991. The Wasatch fault zone, Utah–Segmentation and history of Holocene earthquakes. *J. Struct. Geol.*, **13**(2), 137–149.

Madariaga, R., Olsen, K., and Archuleta, R. 1998. Modeling dynamic rupture in a 3D earthquake fault model. *Bull. seism. Soc. Am.*, **88**(5), 1182.

Magistrale, H., and Day, S. 1999. 3D simulations of multi-segment thrust fault rupture. *Geophys. Res. Lett.*, **26**(14), 2093–2096.

Magistrale, H., Day, S.M, Clayton, R.W., and Graves, R. 2000. The SCEC Southern California Reference Three-Dimensional Seismic Velocity Model Version 2. *Bull. Seism. Soc. Am.*, **90**(6B), S65–S76.

Magistrale, H., Olsen, K., and Pechmann, J. 2008. *Construction and Verification of a Wasatch Front Community Velocity Model: Collaborative Research with San Diego State University and the University of Utah.* Final Technical Report submitted to NEHRP. U.S. Geological Survey.

Magistrale, H., Pechmann, J.C., and Olsen, K.B. 2009. The Wasatch Front, Utah, community seismic velocity model. *Seism. Res. Lett.*, **80**, 368.

Mai, P. M., and Beroza, G. C. 2002. A spatial random field model to characterize complexity in earthquake slip. *Journal of Geophysical Research (Solid Earth)*, **107**(Nov.), 2308–+.

Mai, P. M., Imperatori, W., and Olsen, K. B. 2010. Hybrid Broadband Ground-Motion Simulations: Combining Long-Period Deterministic Synthetics with High-Frequency Multiple S-to-S Backscattering. *Bull. seism. Soc. Am.*, **100**(5A), 2124–2142.

Mai, P.M., and Beroza, G.C. 2003. A hybrid method for calculating near-source, broadband seismograms: application to strong motion prediction. *Phys. Earth Planet. Int.*, **137**, 183–199.

Mai, P.M., Spudich, P., and Boatwright, J. 2005. Hypocenter locations in finite-source rupture models. *Bulletin of the Seismological Society of America*, **95**(3), 965.

Masing, G. 1926. Eigenspannungen und Verfestigung beim Messing. *In: Proc. 2nd Int. Congress of Applied Mechanics, Zürich*, vol. 332.

McCalpin, J., and Nelson, C. 2000. *Long recurrence records from the Wasatch fault zone.* Final technical report. U.S. Geological Survey, National Earthquake Hazards Reduction Program, Contract number 99HQGR0058.

McCalpin, J.P., and Nishenko, S.P. 1996. Holocene paleoseismicity, temporal clustering, and probabilities of future large (M>7) earthquakes on the Wasatch fault zone, Utah. *J. Geophys. Res.*, **101**, 6233–6253.

McDonald, G.N., and Ashland, F.X. 2008. *Earthquake site conditions in the Wasatch Front urban corridor, Utah.* Special Study 125. Utah Geol. Surv.

Mena, B., Durukal, E., and Erdik, M. 2006. Effectiveness of Hybrid Green's Function Method in the Simulation of Near-Field Strong Motion: An Application to the 2004 Parkfield Earthquake. *Bull. seism. Soc. Am.*, **96**(4B), S183–205.

Mena, B., Mai, P. M., Olsen, K. B., Purvance, M. D., and Brune, J. N. 2010. Hybrid Broadband Ground-Motion Simulation Using Scattering Green's Functions: Application to Large-Magnitude Events. *Bull. seism. Soc. Am.*, **100**(5A), 2143–2162.

Murphy, M., Benz, H., Hill, J.A., and Schuster, G.T. 1988. Prediction of seismic amplification due to resonance of P-SV and SH waves in Salt Lake Valley, Utah. *Seism. Res. Lett.*, **59**, 10–11.

O'Connell, D. R. H., Ma, S., and Archuleta, R. J. 2007. Influence of Dip and Velocity Heterogeneity on Reverse- and Normal-Faulting Rupture Dynamics and Near-Fault Ground Motions. *Bull. seism. Soc. Am.*, **97**(6), 1970–1989.

Olsen, K. B. 1994. *Simulation of three-dimensional wave propagation in the Salt Lake Basin.* Ph.D. thesis, University of Utah, Salt Lake City, Utah.

Olsen, K. B., and Schuster, G.T. 1995. Causes of low-frequency ground motion amplification in the Salt Lake basin: The case of the vertically incident P wave. *Geophys. J. Int.*, **122**(3), 1045–1061.

Olsen, K. B., Day, S. M., Dalguer, L. A., Mayhew, J., Cui, Y., Zhu, J., Cruz-Atienza, V., Roten, D., Maechling, P., Jordan, T., Okaya, D., and Chourasia, A. 2009. ShakeOut-D: Ground Motion Estimates Using an Ensemble of Large Earthquakes on the Southern San Andreas Fault With Spontaneous Rupture Propagation. *Geophys. Res. Lett.*, **36**, L04303.

Olsen, K.B., and Archuleta, R.J. 1996. Three-dimensional simulation of earthquakes on the Los Angeles fault system. *Bull. seism. Soc. Am.*, **86**(3), 575–596.

Olsen, K.B., and Schuster, G.T. 1994. *Three-dimensional modeling of the site amplification in East Great Salt Lake Basin.* Technical Report 1434-93-G-2345. U.S. Geol. Surv.

Olsen, K.B., Pechmann, J.C., and Schuster, G.T. 1996. An analysis of simulated and observed blast records in the Salt Lake Basin. *Bull. Seism. Soc. Am.*, **86**, 1061–1076.

Olsen, Kim B., Pechmann, James C., and Schuster, Gerard T. 1995. Simulation of 3D elastic wave propagation in the Salt Lake Basin. *Bull. Seism. Soc. Am.*, **85**(6), 1688–1710.

OpenSHA. 2010. Open Seismic Hazard Analysis Computer Platform. *http://www.opensha.org/.*

Pitarka, A., Irikura, K., Iwata, T., and Sekiguchi, H. 1998. Three-dimensional simulation of the near-fault ground motion for the 1995 Hyogo-Ken Nanbu (Kobe), Japan, earthquake. *Bull. seism. Soc. Am.*, **88**(2), 428–440.

Pitarka, A., Somerville, P., Fukushima, Y., Uetake, T., and Irikura, K. 2000. Simulation of Near-Fault Strong-Ground Motion Using Hybrid Green's Functions. *Bull. seism. Soc. Am.*, **90**(3), 566–586.

Press, W.H., Teukolsky, S.A., Vetterling, W.T., and Flannery, B.P. 2007. *Numerical Recipes: The Art of Scientific Computing.* 3rd edn. Cambridge University Press.

Pyke, R.M. 1979. Nonlinear soil models for irregular cyclic loadings. *Journal of the Geotechnical Engineering Division*, **105**(6), 715–726.

Ripperger, J., Ampuero, J.-P., Mai, P. M., and Giardini, D. 2007. Earthquake source characteristics from dynamic rupture with constrained stochastic fault stress. *Journal of Geophysical Research (Solid Earth)*, **112**(B11), 4311–+.

Ripperger, J., Mai, PM, and Ampuero, J.P. 2008. Variability of near-field ground motion from dynamic earthquake rupture simulations. *Bull. seism. Soc. Am.*, **98**(3), 1207.

Roten, D., Fäh, D., Olsen, K.B., and Giardini, D. 2008. A comparison of observed and simulated site response in the Rhône valley. *Geophys. J. Int.*, **173**(June), 958–978.

Roten, D., Fäh, D., Bonilla, LF, Alvarez-Rubio, S., Weber, TM, and Laue, J. 2009. Estimation of non-linear site response in a deep Alpine valley. *Geophys. J. Int.*, **178**(3), 1597–1613.

Roten, D., Fäh, D., and Laue, J. 2011. Application of a neighborhood algorithm for parameter identification in a cyclic mobility model. *In: 4th IASPEI/IAEE International Symposium: Effects of Surface Geology on Seismic Motion, August 23-26, 2011, University of Santa Barbara*.

Schmedes, J., Archuleta, R.J., and Lavallée, D. 2010. Correlation of earthquake source parameters inferred from dynamic rupture simulations. *J. Geophys. Res*, **115**.

Schnabel, P., Seed, H. Bolton, and Lysmer, J. 1972. Modification of seismograph records for effects of local soil conditions. *Bull. Seism. Soc. Am.*, **62**(6), 1649–1664.

Scholz, C.H. 1998. Earthquakes and friction laws. *Nature*, **391**(6662), 37–42.

Schroeder, W., Martin, K., and Lorsensen, B. 2006. *The visualization toolkit: an object-oriented approach to 3D graphics*. 4 edn. Kitware, Clifton Park, N.Y.

Sibson, R.H. 1991. Loading faults to failure. *Bull. Seism. Soc. Am.*, **81**(6), 2493–2497.

Silva, W.J., Wong, I.G., and Darragh, R.B. 1998. Engineering characterization of earthquake strong ground motions in the Pacific Northwest. *Pages 313–324 of:* Rogers, A.M., Walsh, T.J., Kockleman, W.J., and Priest, G.R. (eds), *Assessing Earthquake Hazards and Reducing Risk in the Pacific Northwest*, vol. 2. U.S. Geological Survey Professional Paper 1560.

Smith, R.B., and Arabasz, W.J. 1991. Seismicity of the Intermountain seismic belt. *Pages 185–228 of:* Slemmons, D.B., Engdahl, E.R., Zoback, M.D., and Blackwell, D.D. (eds), *Neotectonics of North America*. Geological Society of America, Boulder, Colorado.

Solomon, B.J., Storey, N., Wong, I., Gregor, N., Wright, D., and McDonald, G. 2004. *Earthquake-hazards scenario for a M7 earthquake on the Salt Lake City segment of the Wasatch fault zone, Utah*. Utah Geol. Surv. Spec. Study 111DM, CD-ROM, 59pp., 6pl.

Somerville, PG, and Pitarka, A. 2006. Differences in earthquake source and ground motion characteristics between surface and buried earthquakes. *In: Proc. of the 8th National Conference on Earthquake Engineering*.

Taborda, R., and Bielak, J. 2008. *Three-dimensional modeling of earthquake ground motion in basins, including nonlinear wave propagation in soils*. Final Technical Report, USGS Award 08HQGR0018.

Towhata, I., and Ishihara, K. 1985. Modeling soil behavior under principal axes rotation. *Pages 523–530 of: Fifth International Conference on Numerical Methods in Geomechanics, Nagoya, Japan*.

Vucetic, M. 1990. Normalized behavior of clay under irregular cyclic loading. *Canadian Geotechnical Journal*, **27**(1), 29–46.

Vucetic, M., and Dobry, R. 1991. Effect of soil plasticity on cyclic response. *J. Geotech. Eng.*, **117**(1), 89–107.

Wells, D.L., and Coppersmith, K.J. 1994. New empirical relationships among magnitude, rupture length, rupture width, rupture area, and surface displacement. *Bull. seism. Soc. Am.*, **84**(4), 974–1002.

Wessel, P., and Smith, W.H.F. 1998. New, improved version of Generic Mapping Tools released. *EOS Trans. AGU*, **79**(47), 579.

Williams, R.A., King, K.W., and Tinsley, J.C. 1993. Site response estimates in Salt Lake Valley, Utah, from borehole seismic velocities. *Bull. seism. Soc. Am.*, **83**(3), 862–889.

Wong, I., Silva, W., Olig, S, Thomas, P., Wright, D., Ashland, N., Gregor, N., Pechmann, M., Dober, M., Christenson, G., and Gerth, R. 2002a. *Earthquake scenario and probabilistic ground shaking maps for the Salt Lake City, Utah, metropolitan area*. Misc. Pub. MP-02-5. Utah Geol. Surv.

Wong, I., Silva, W., Gregor, N., Wright, D., Ashland, F., McDonald, G., Olig, S., Christenson, G., and Solomon, B. 2002b. Earthquake scenario ground shaking maps for the central Wasatch Front, Utah. *In: Proceedings of the 7th U.S. National Conference on Earthquake Engineering, Boston, Mass., July 21-25, 2002.*

Wong, I.G., and Silva, W.J. 1993. *Site-specific strong ground motion estimates for the Salt Lake Valley, Utah.* Misc. Pub.93-9. Utah Geol. Surv.

Wong, I.G., Silva, W.J., Pechmann, J.C., Darragh, R.B., and Yu, T. 2011. *Analyses of Earthquake Source, Path, and Site Factors From ANSS Data Along the Wasatch Front, Utah.* Final Technical Report, USGS Award 05HQGR0010.

Zeghal, M., and Elgamal, A.W. 1994. Analysis of site liquefaction using earthquake records. *Journal of Geotechnical Engineering;(United States)*, **120**(6).

Zeng, Y. 1993. Theory of scattered P- and S-wave energy in a random isotropic scattering medium. *Bull. seism. Soc. Am.*, **83**(4), 1264–1276.

Zeng, Y., Su, F., and Aki, K. 1991. Scattering Wave Energy Propagation in a Random Isotropic Scattering Medium 1. Theory. *J. Geophys. Res.*, **96**(B1), 607–619.

Zeng, Y., Anderson, J. G., and Feng, S. 1995. Subevent rake and random scattering effects in realistic ground motion simulation. *Geophys. Res. Lett.*, **22**(1), 17–20.

Figure Captions

Figure 1: Map of the Salt Lake basin showing known Quaternary surface faulting on the Wasatch fault zone and the surface trace of the WFSLC model. The mesh shows the 3D structure of the WFSLC with along-strike and along-dip distances in 1000 m contours. Letters represent the epicenter locations in the six rupture models. The outer rectangle shows the extent of the computational model used for FD simulations; the inner rectangle indicates the region shown in Figure 2. WSF=Warms Springs fault, EBF=East Bench fault, CS=Cottonwood section.

Figure 2: *Left panel:* Cross-sections through the WFCVM in the central Salt Lake basin (inner rectangle in Fig. 1) showing the shear-wave velocity ($\mathrm{m{\cdot}s^{-1}}$). The gray surface shows the WFSLC model. The depth scale is in meters. *Right panel:* V_{S30} for sediments (color coded) and depth to the base of the unconsolidated sediments R_1 (100 m contours).

Figure 3: Distribution of dynamic rupture parameters on the fault for rupture model B. *Left panels:* Initial shear stress τ_0 and normal stress σ_n. *Center panels:* Strength excess $\tau_{cs} - \tau_0$ and dynamic stress drop $\Delta\tau = \tau_0 - \tau_{cd}$. *Upper right panel:* Static and dynamic coefficients of friction (μ_s and μ_d, respectively) and critical slip distance d_0 as a function of depth. *Lower right panel:* Static and dynamic failure stress (τ_{cs} and τ_{cd}), initial normal stress σ_n and initial shear stress τ_0 as a function of depth at 25 km along-strike distance.

Figure 4: Static slip, rupture times and peak slip rates obtained from the four rupture models.

Figure 5: Rotation-independent horizontal 2s-SAs for all six scenarios.

Figure 6: Geometric mean of 2s-SAs and 3s-SAs *(left)* and geometric standard deviation σ *(right)* from the six scenarios. Note the different scale for the mean 2s-SAs compared to Figure 5.

Figure 7: *Left panel:* Joyner-Boore distance R_{JB} (black contours) and areas used for comparison with BA08, where 200 $\mathrm{m{\cdot}s^{-1}} \leq V_{S30} \leq$ 300 $\mathrm{m{\cdot}s^{-1}}$ (highlighted areas). *Right panels:* Geometric mean of 3s-SAs and 2s-SAs obtained from the ensemble of rupture models including the geometric standard deviation (error bars). Solid lines show the predictions according to BA08, and dashed lines show the geometric standard deviation. The histogram on the lower right shows the number of samples in each distance bin.

Figure 8: Same as Figure 7, but showing comparisons to CB08, AS08 and CY08 as a function of R_{Rup} (black contours on the map) for $R_{\mathrm{JB}} = 0$. The straight black lines mark the locations of the cross-sections shown in Figure 18.

Figure 9: Same as Figures 7 and 8, but showing comparisons with the four NGA models for bedrock sites on the footwall.

Figure 10: Map of the Salt Lake basin showing the distribution of site response units inside the computational area and the location of the three cross-sections used for nonlinear simulations. The thick white line along the Wasatch Front represents the surface rupture of the WFSLC. Green letters represent the epicenter locations in the six rupture models. Modified from McDonald and Ashland (2008).

Figure 11: Typical shear stress-strain relationship of soil under cyclic loads for a hyperbolic model. Backbone and reloading curves were computed from equations 16 and 17 ($\kappa_H = 2$) using a reference strain γ_r of 0.1% and two different values for the shear modulus G_0, corresponding to shear-wave velocities of 250 and 300 m·s^{-1} and a density of 2000 kgm^{-3}. The pair (γ_t, τ_t) represents the point where the path reverses from loading to unloading. Modified from Bonilla (2001).

Figure 12: Reference strain γ_r (solid line) and $\gamma_r \pm \sigma$ (dashed lines) as a function of depth derived from Darendeli (2001) for site P1-100 (Fig. 10). The symbols show γ_r determined by Bay and Sasanakul (2005) from torsional shear tests at the depth corresponding to the applied confining pressure.

Figure 13: Test of different boundary conditions (BCs) in NOAH. The upper panels show the original BB synthetic on the free surface (cyan), which was deconvolved to represent a borehole record at 240 m depth (blue) and then propagated back to the surface (black) using rigid BCs in NOAH. The bottom panel shows the same experiment, but deconvolving to outcrop conditions of 240 m depth and dividing the resulting signal by 2, and propagating the result back up to the surface using transmitting (elastic) BCs at 240m depth. Fourier spectra (right panels) were smoothed using the method defined by Konno and Ohmachi (1998) with b=40.

Figure 14: Comparison of LF (thick lines) and BB (thin lines) velocity synthetics (top) and corresponding Fourier spectra (bottom) for source model B' at three selected strong motion sites in the SLB: SLC international airport (2287), downtown SLC (2289) and Butlerville substation (BSS). A Konno-Ohmachi window (b=80) was used to smooth the Fourier spectra. The numbers on the time-domain records denote peak velocity in m·s^{-1}.

Figure 15: *Top panels:* 0.2s-SAs predicted by four NGA equations and computed from linear BB synthetics along profile P0 for source model B *(top left)* and along profile P1 for source model B' *(top right)*. See Figure 10 for profile locations. The thin black lines show the largest median plus one standard deviation and the smallest median minus one standard deviation of all four considered NGA Models. *Bottom panels*: Cross-sections through the WFCVM showing the shear-wave velocity. The black lines indicate the fault.

Figure 16: Example of 1-D nonlinear simulation for site P1-100 (Fig. 10) showing the E-W component from rupture model B'. *(A):* Acceleration time series of linear BB ground motion, deconvolved linear BB signal used as input signal, and ground motion on the top of the nonlinear layer. *(B):* Response spectra of time series depicted in (A). *(C):* Peak shear strain encountered during the simulation (solid) and reference strain (dashed) as a function of depth. *(D):* Peak acceleration as a function of depth. *(E):* Shear-wave velocity profile. *(F):* Shear stress τ_{xy} versus strain γ_{xy} at different depths.

Figure 17: Same as Figure 15, but showing SAs derived from fully nonlinear 1-D simulations. The hatched areas depict SAs obtained from the upper- and lower-bound nonlinear models, using $(\gamma_r - \sigma,\ \xi_{\max} + \sigma_r)$ and $(\gamma_r + \sigma,\ \xi_{\max} - \sigma_r)$, respectively.

Figure 18: Average sediment-to-bedrock spectral acceleration ratios for five different fre-

quencies along the two cross-sections indicated in Figure 8. The triangle shows the location of the bedrock site used for the normalization.

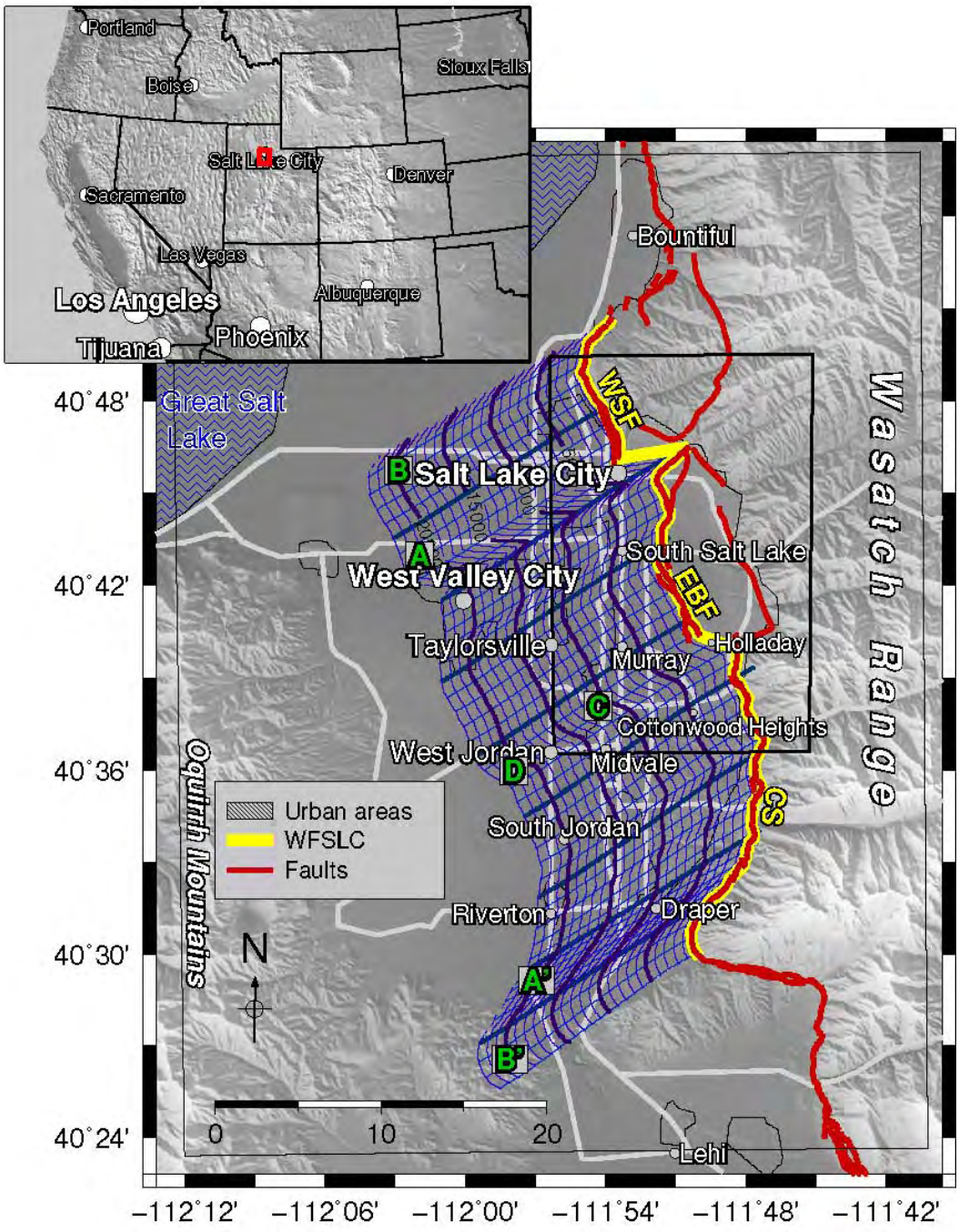
Portland
Boise
Sioux Falls
Salt Lake City
Denver
Sacramento
Las Vegas
Albuquerque
Los Angeles
Phoenix
Tijuana
Great Salt Lake
Bountiful
WSF
B Salt Lake City
A
West Valley City
South Salt Lake
EBF
Taylorsville
Murray
Holladay
C
Cottonwood Heights
West Jordan
D
Midvale
CS
South Jordan
Riverton
Draper
A'
B'
Lehi
Wasatch Range
Oquirrh Mountains
Urban areas
WFSLC
Faults
N
0
10
20
40°48'
40°42'
40°36'
40°30'
40°24'
−112°12'
−112°06'
−112°00'
−111°54'
−111°48'
−111°42'

Figure 1:

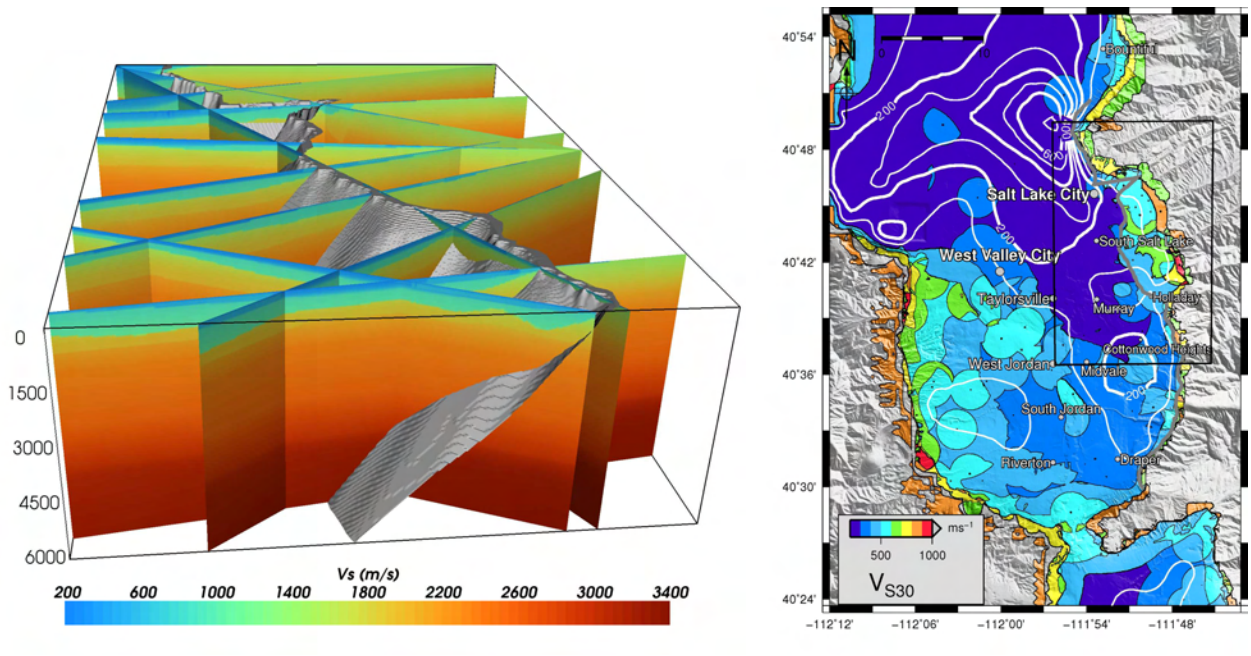

Figure 2:

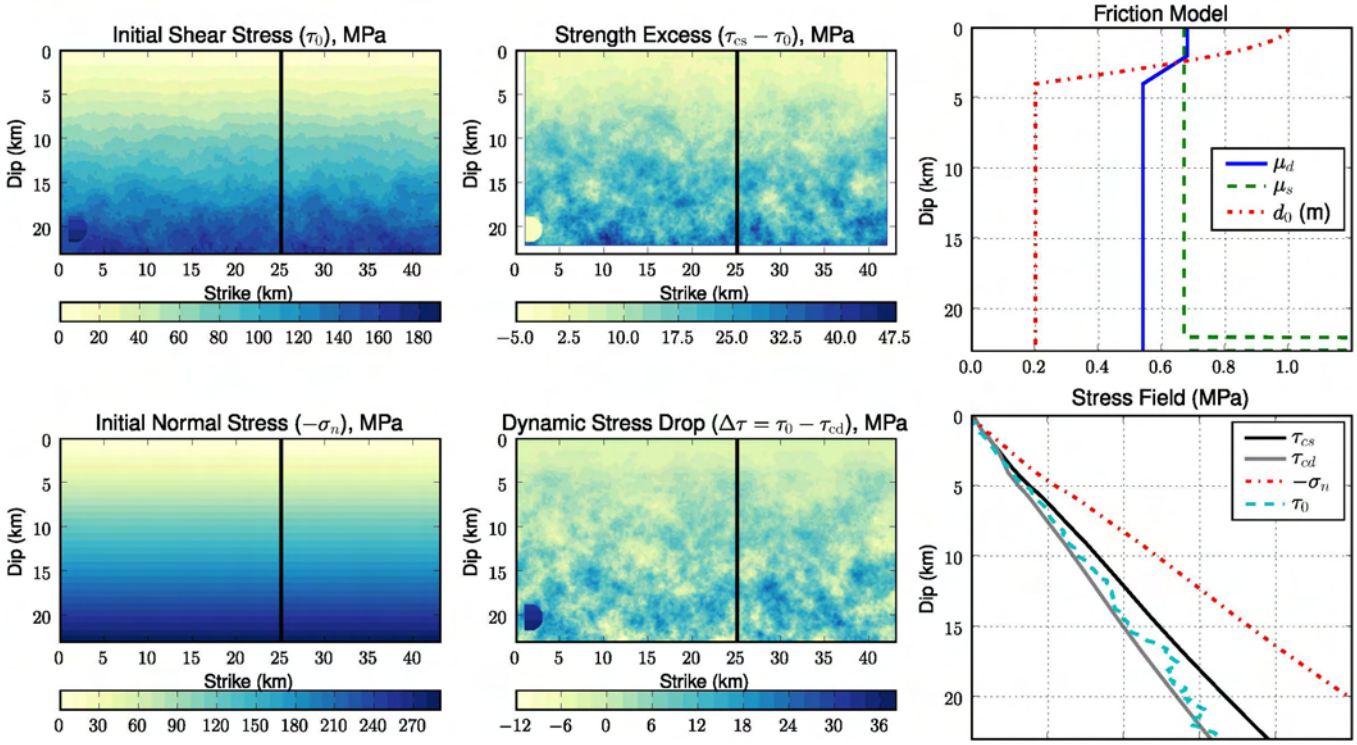

Figure 3:

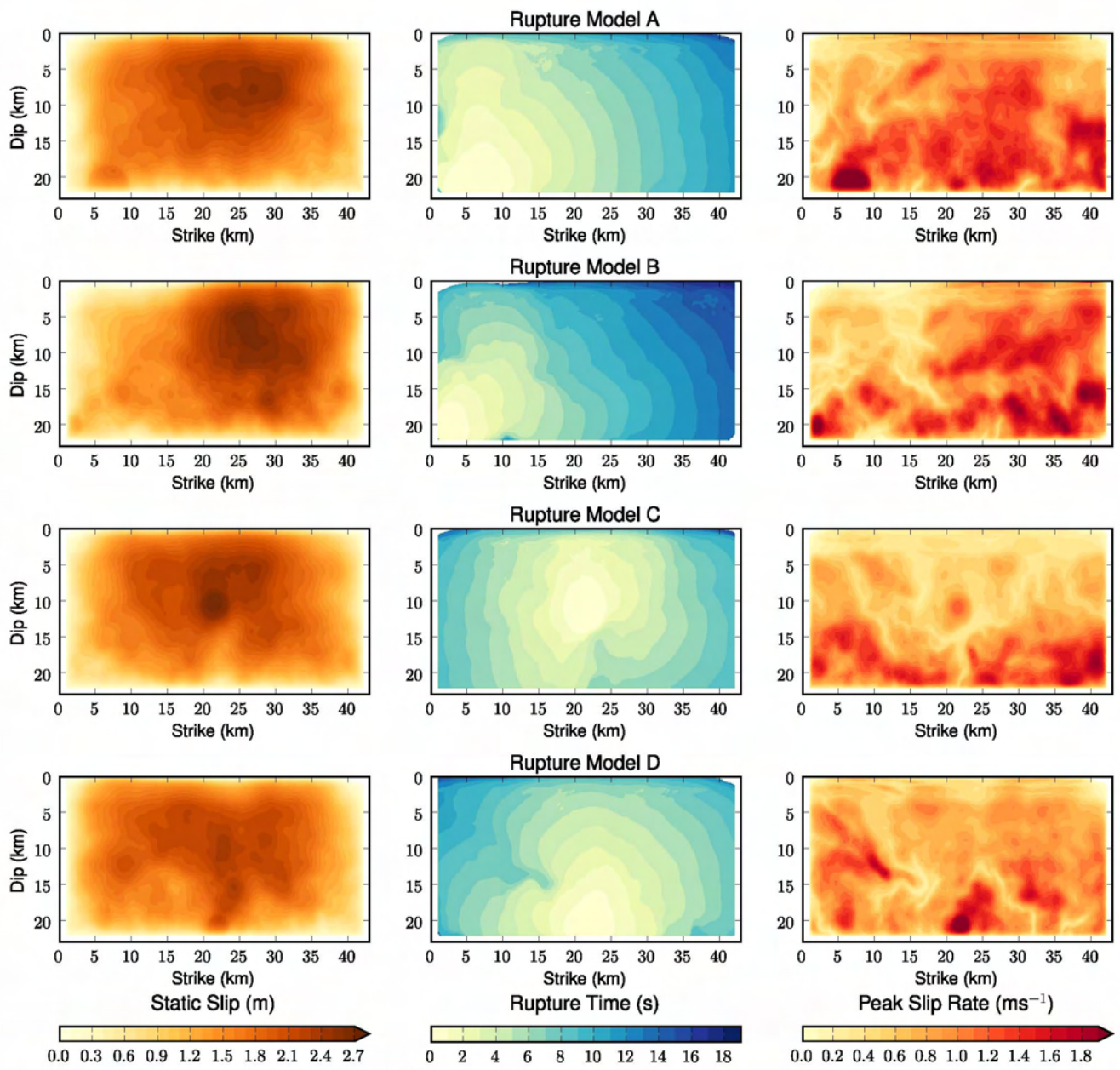
Rupture Model A
Rupture Model B
Rupture Model C
Rupture Model D
Dip (km)
Strike (km)
Static Slip (m)
0.0 0.3 0.6 0.9 1.2 1.5 1.8 2.1 2.4 2.7
Rupture Time (s)
0 2 4 6 8 10 12 14 16 18
Peak Slip Rate (ms^{-1})
0.0 0.2 0.4 0.6 0.8 1.0 1.2 1.4 1.6 1.8

Figure 4:

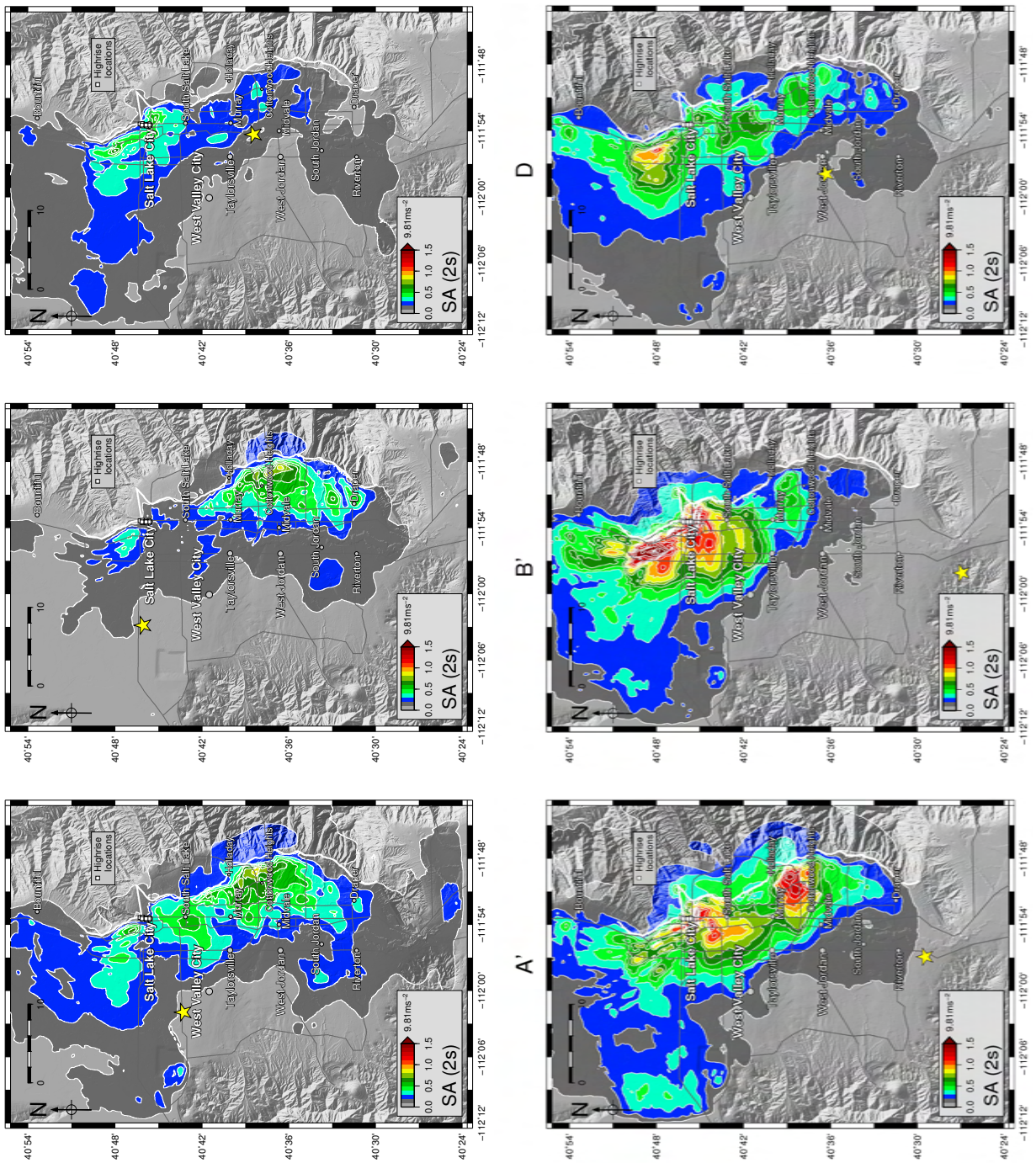
A
B
C
A'
B'
D
Boundary
Highrise locations
Salt Lake City
West Valley City
Taylorsville
Murray
South Salt Lake
Millcreek
Cottonwood Heights
Midvale
West Jordan
South Jordan
Riverton
Draper
N
0
10
SA (2s)
0.0 0.5 1.0 1.5
9.81ms⁻²
40°54'
40°48'
40°42'
40°36'
40°30'
40°24'
-112°12'
-112°06'
-112°00'
-111°54'
-111°48'

Figure 5:

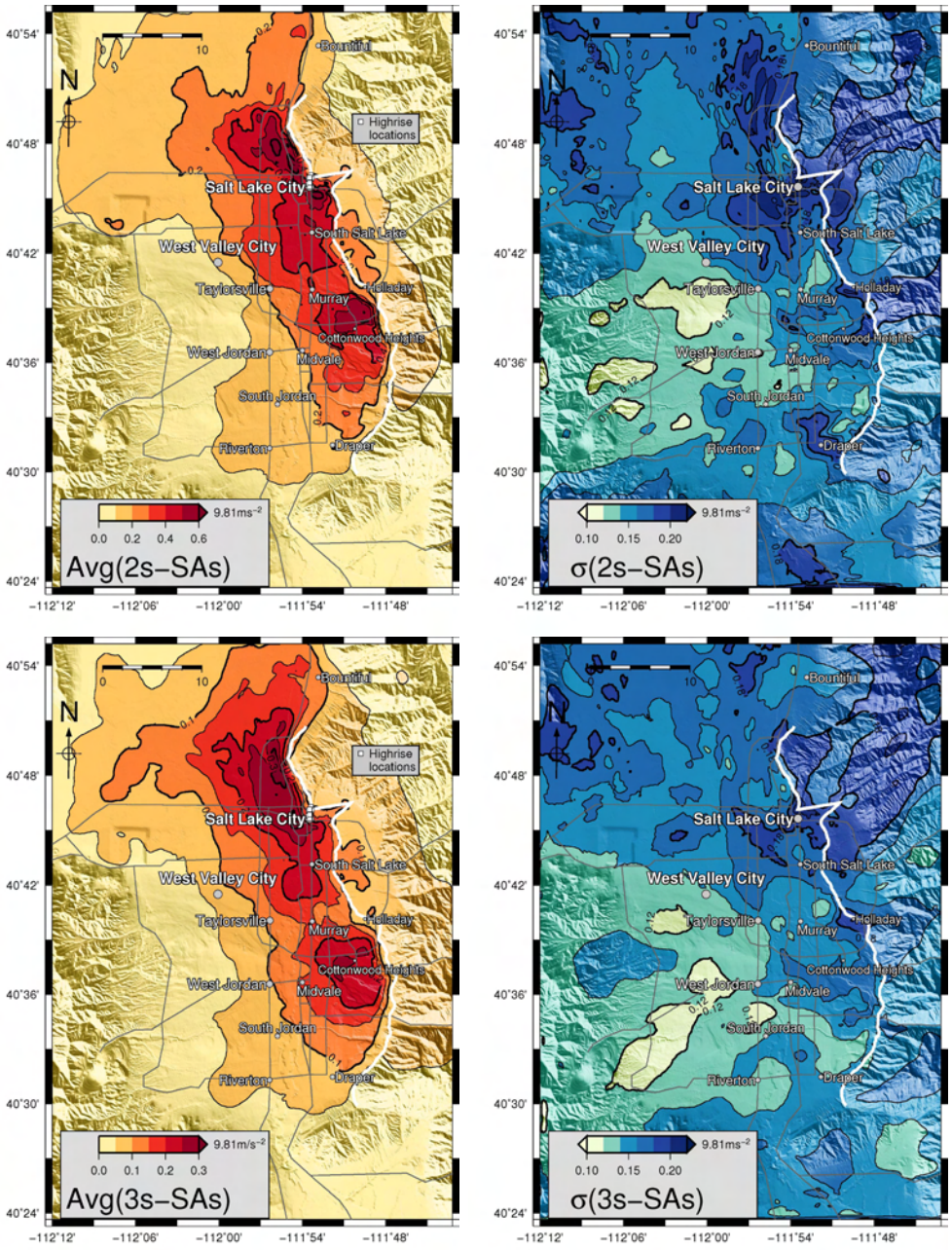
Avg(2s–SAs)
σ(2s–SAs)
Avg(3s–SAs)
σ(3s–SAs)
Highrise locations
Salt Lake City
West Valley City
Bountiful
South Salt Lake
Taylorsville
Murray
Holladay
Cottonwood Heights
West Jordan
Midvale
South Jordan
Riverton
Draper
9.81ms⁻²
9.81m/s⁻²
N

Figure 6:

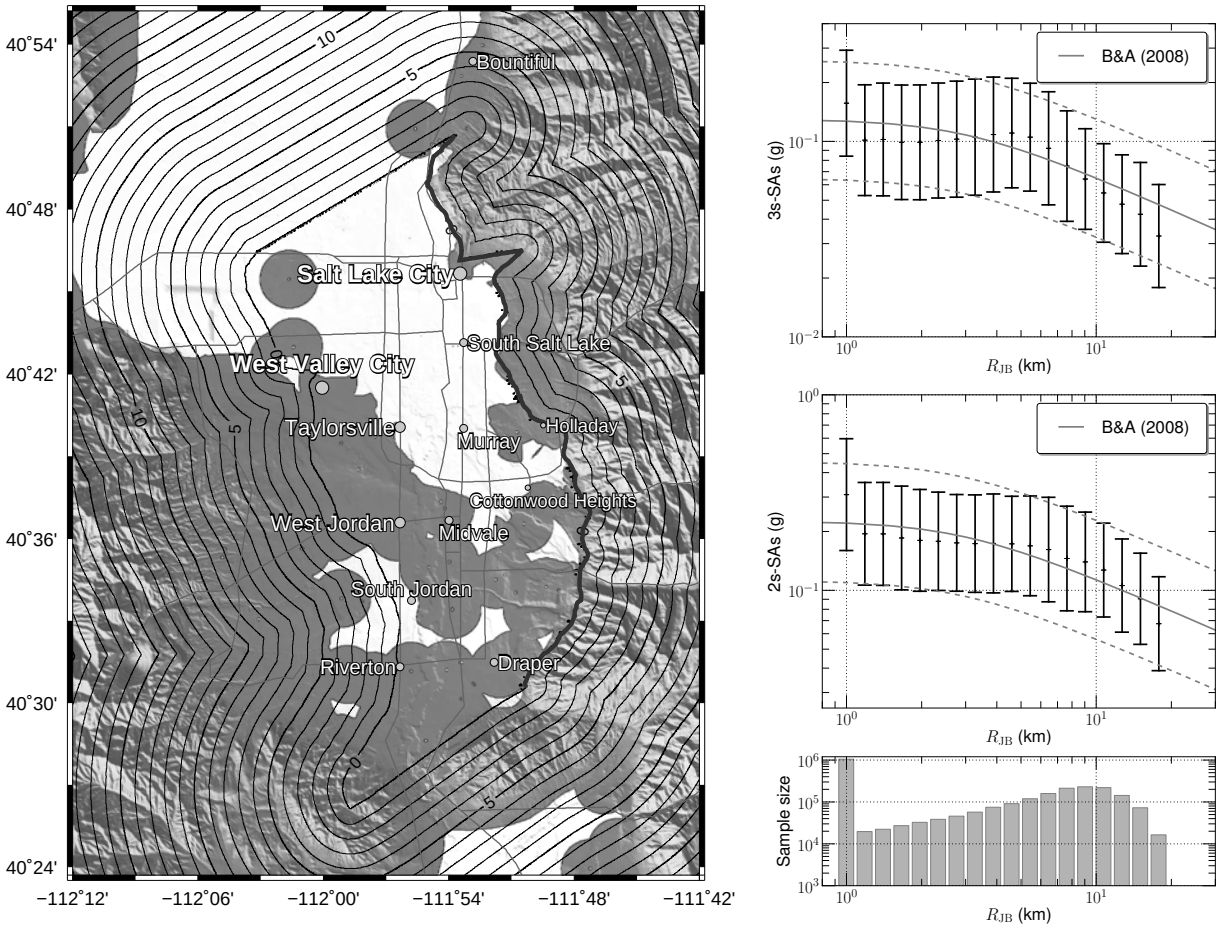
40˚54'
40˚48'
40˚42'
40˚36'
40˚30'
40˚24'
−112˚12'
−112˚06'
−112˚00'
−111˚54'
−111˚48'
−111˚42'
Bountiful
Salt Lake City
South Salt Lake
West Valley City
Taylorsville
Murray
Holladay
Cottonwood Heights
West Jordan
Midvale
South Jordan
Riverton
Draper
10
5
0
B&A (2008)
3s-SAs (g)
2s-SAs (g)
Sample size
R_{JB} (km)

Figure 7:

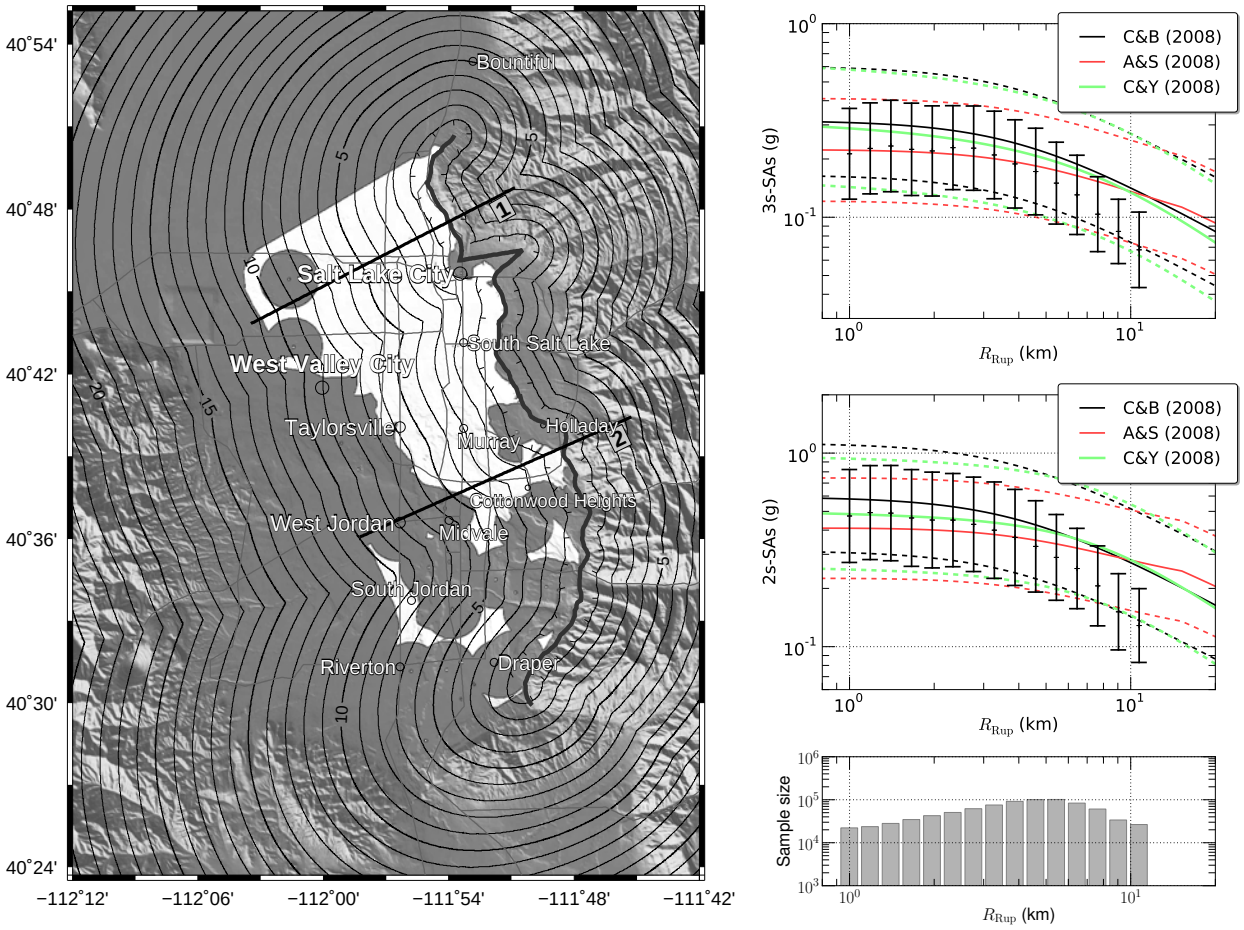
40°54'
40°48'
40°42'
40°36'
40°30'
40°24'
−112°12'
−112°06'
−112°00'
−111°54'
−111°48'
−111°42'
Bountiful
Salt Lake City
West Valley City
South Salt Lake
Taylorsville
Murray
Holladay
Cottonwood Heights
West Jordan
Midvale
South Jordan
Riverton
Draper
C&B (2008)
A&S (2008)
C&Y (2008)
3s-SAs (g)
2s-SAs (g)
Sample size
R_{Rup} (km)

Figure 8:

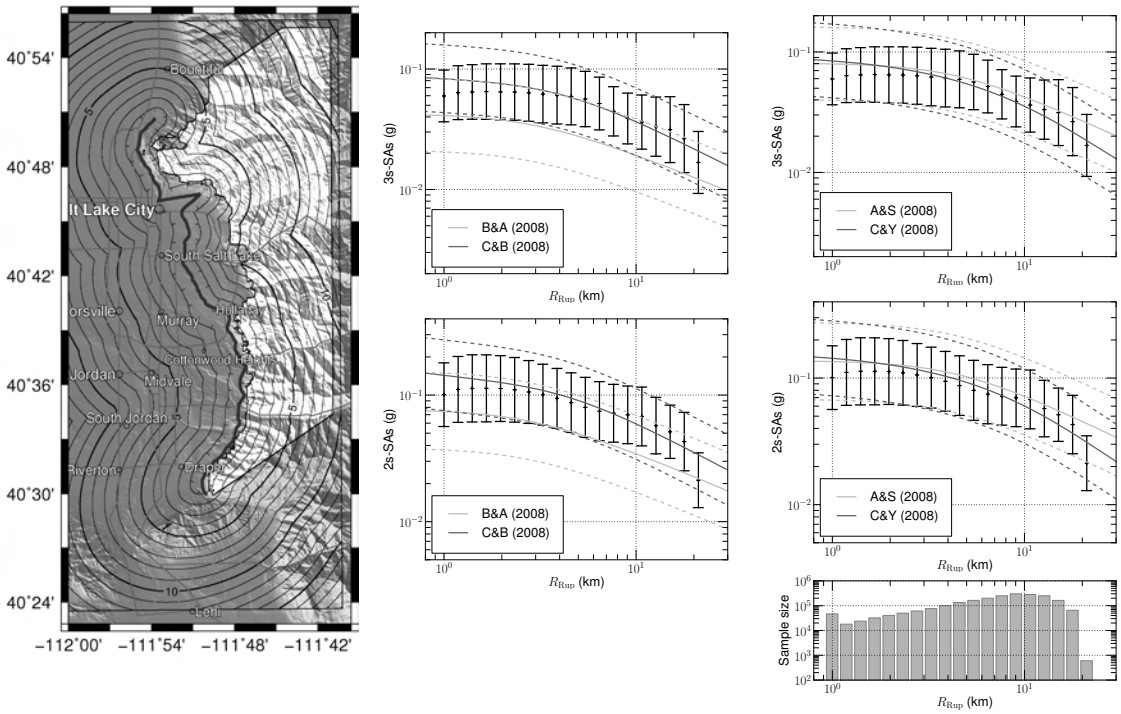
40°54'
40°48'
40°42'
40°36'
40°30'
40°24'
−112°00'
−111°54'
−111°48'
−111°42'
Bountiful
lt Lake City
South Salt Lake
orsville
Murray
Jordan
Midvale
South Jordan
Riverton
Draper
Lehi
3s-SAs (g)
2s-SAs (g)
B&A (2008)
C&B (2008)
A&S (2008)
C&Y (2008)
R_{Rup} (km)
Sample size

Figure 9:

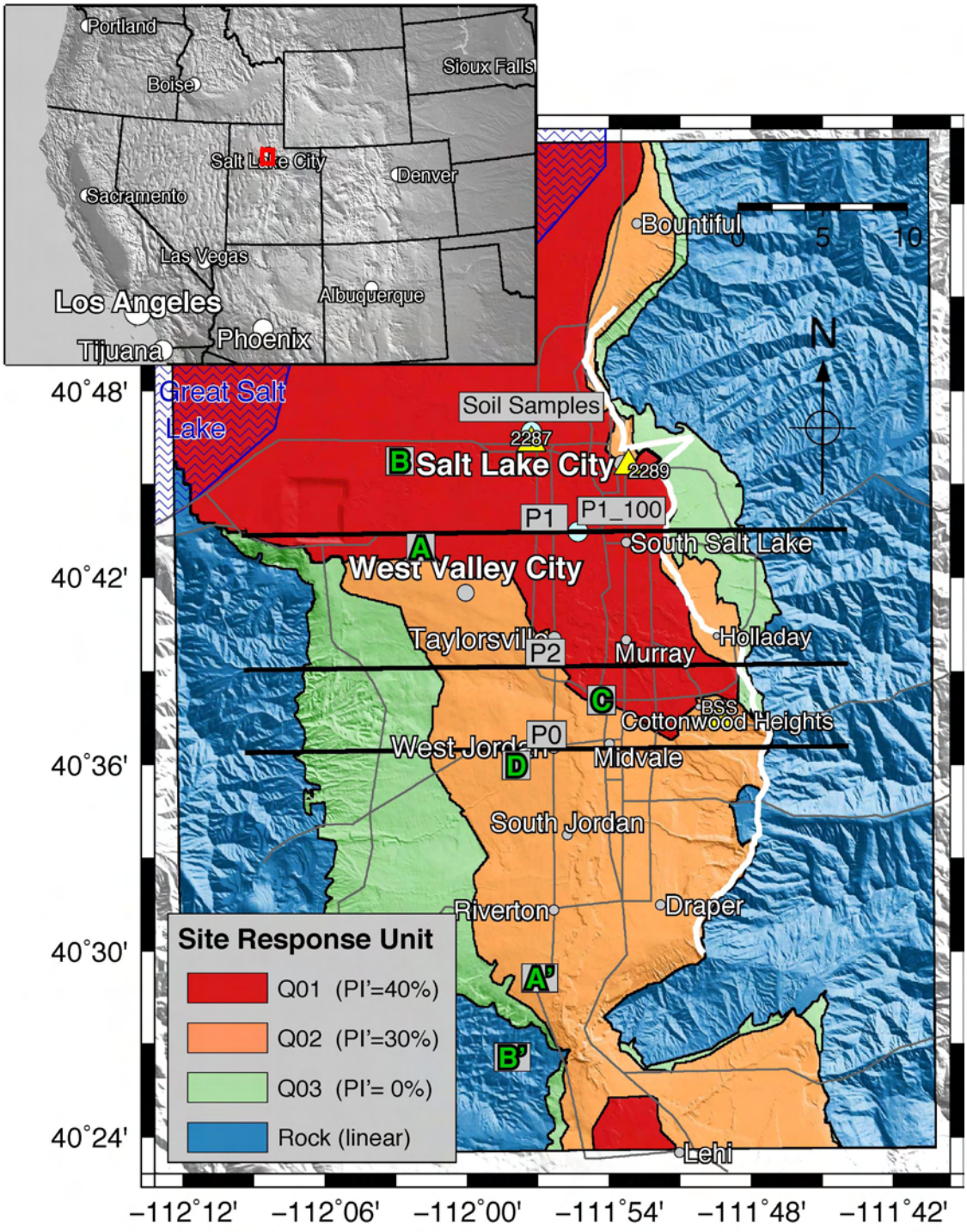
Portland
Boise
Sioux Falls
Salt Lake City
Denver
Sacramento
Las Vegas
Los Angeles
Albuquerque
Phoenix
Tijuana
Great Salt Lake
Soil Samples
2287
2289
B Salt Lake City
P1
P1_100
South Salt Lake
A
West Valley City
Taylorsville
P2
Murray
Holladay
C
BSS
Cottonwood Heights
P0
West Jordan
D
Midvale
South Jordan
Riverton
Draper
A'
B'
Lehi
Bountiful
0
5
10
N
40°48'
40°42'
40°36'
40°30'
40°24'
−112°12'
−112°06'
−112°00'
−111°54'
−111°48'
−111°42'
Site Response Unit
Q01 (PI'=40%)
Q02 (PI'=30%)
Q03 (PI'= 0%)
Rock (linear)

Figure 10:

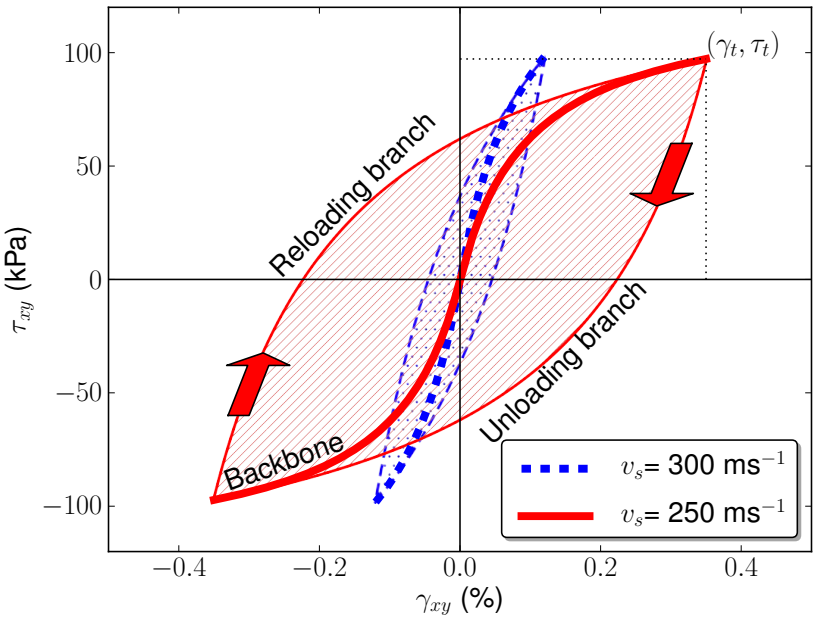

Figure 11:

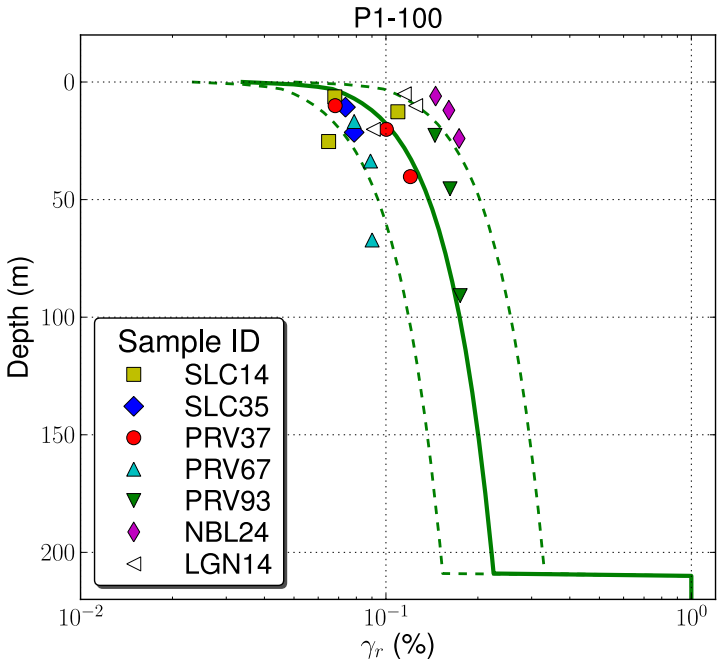

Figure 12:

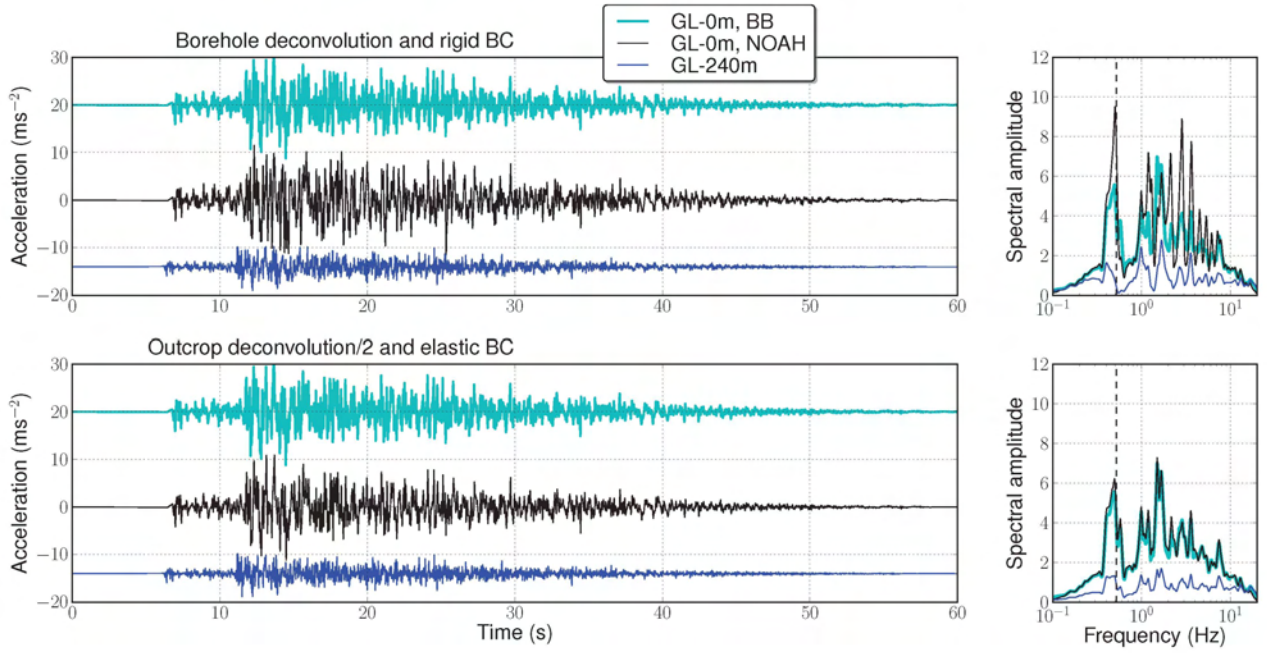

Figure 13:

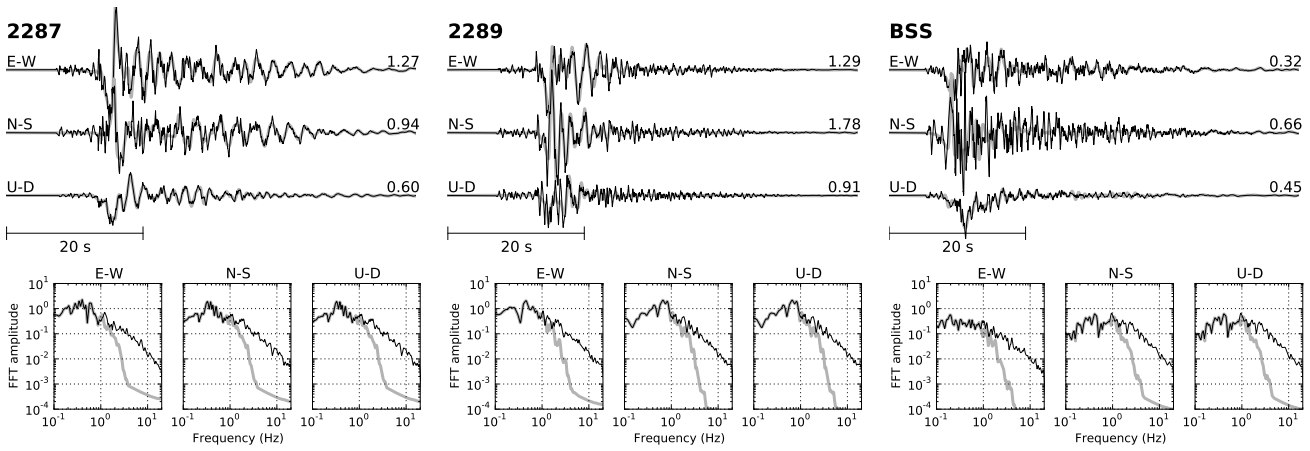

Figure 14:

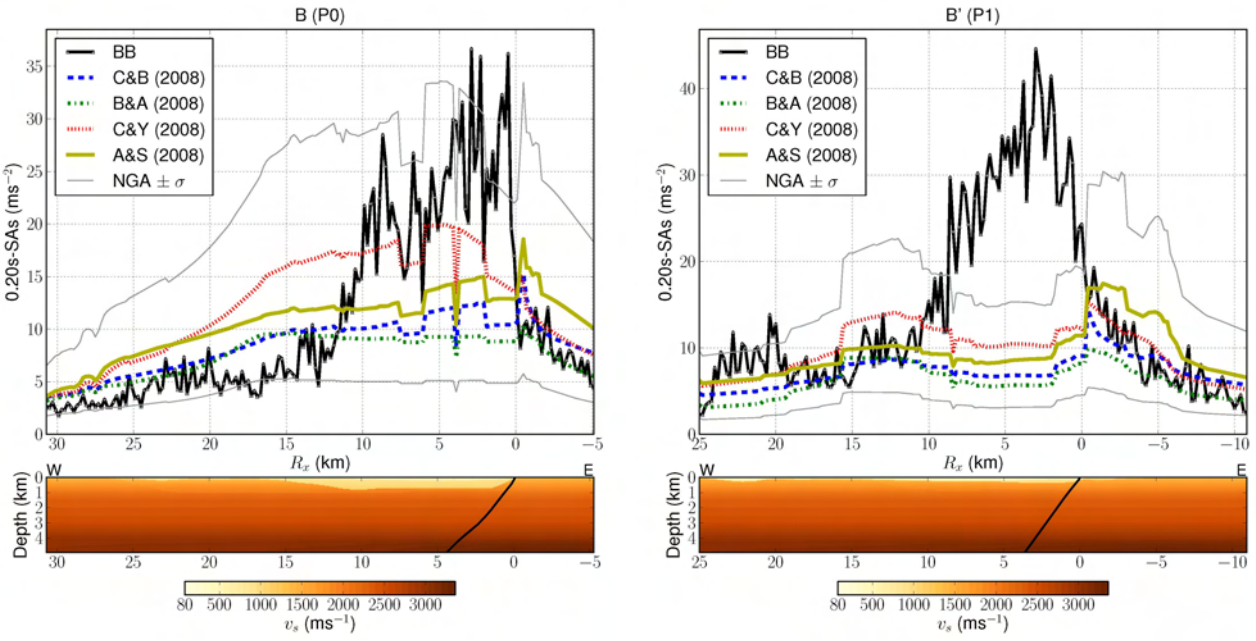
B (P0)
B' (P1)
BB
C&B (2008)
B&A (2008)
C&Y (2008)
A&S (2008)
NGA ± σ
0.20s-SAs (ms⁻²)
R_x (km)
W
E
Depth (km)
80 500 1000 1500 2000 2500 3000
v_s (ms⁻¹)

Figure 15:

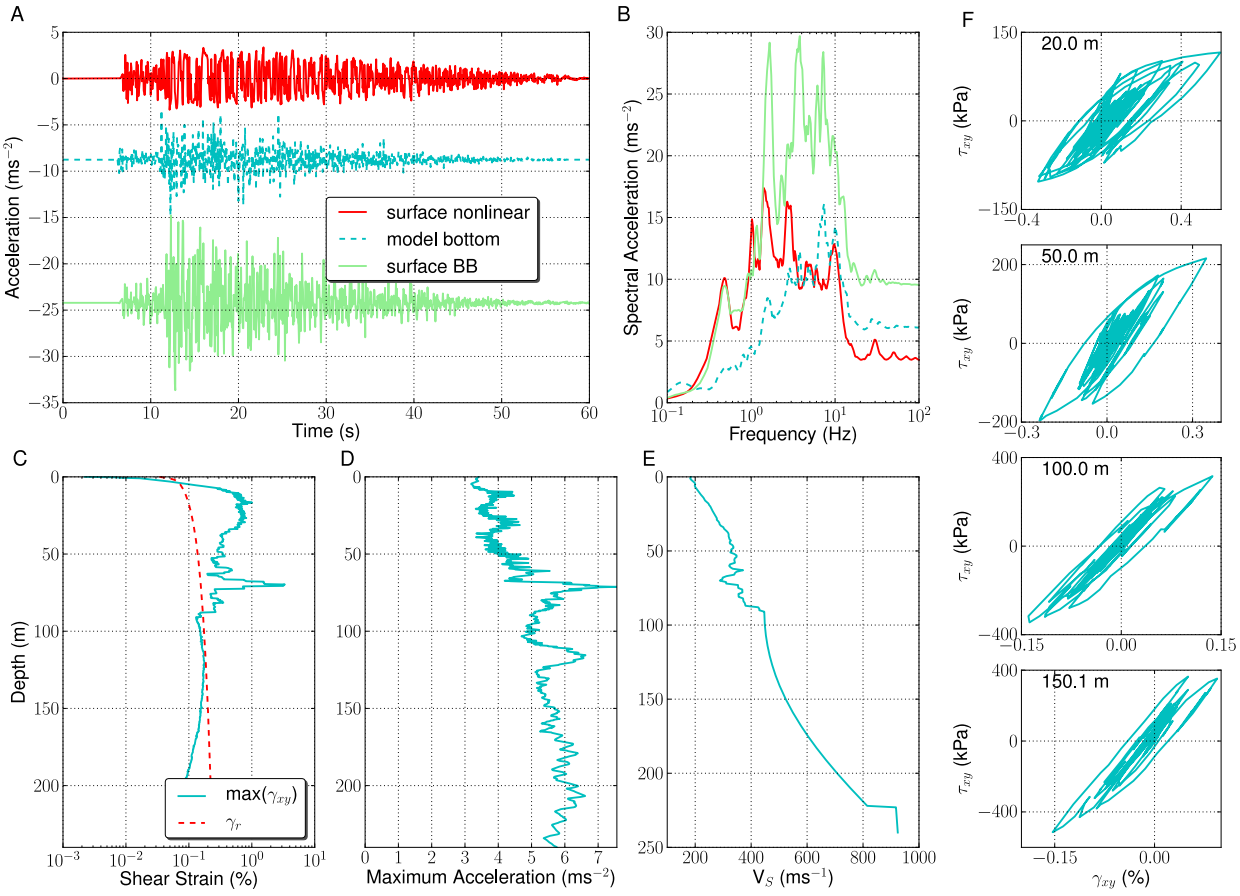
A
Acceleration (ms^{-2})
Time (s)
surface nonlinear
model bottom
surface BB
B
Spectral Acceleration (ms^{-2})
Frequency (Hz)
C
Depth (m)
Shear Strain (%)
max(γ_{xy})
γ_r
D
Maximum Acceleration (ms^{-2})
E
V_S (ms^{-1})
F
20.0 m
50.0 m
100.0 m
150.1 m
τ_{xy} (kPa)
γ_{xy} (%)

Figure 16:

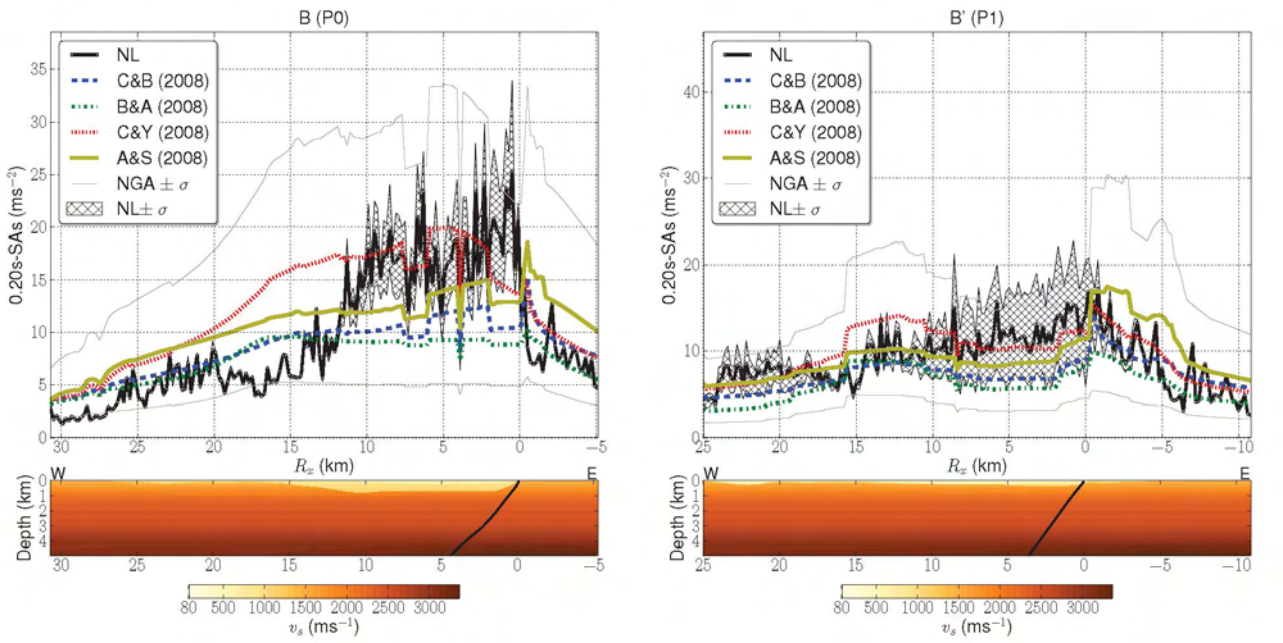

Figure 17:

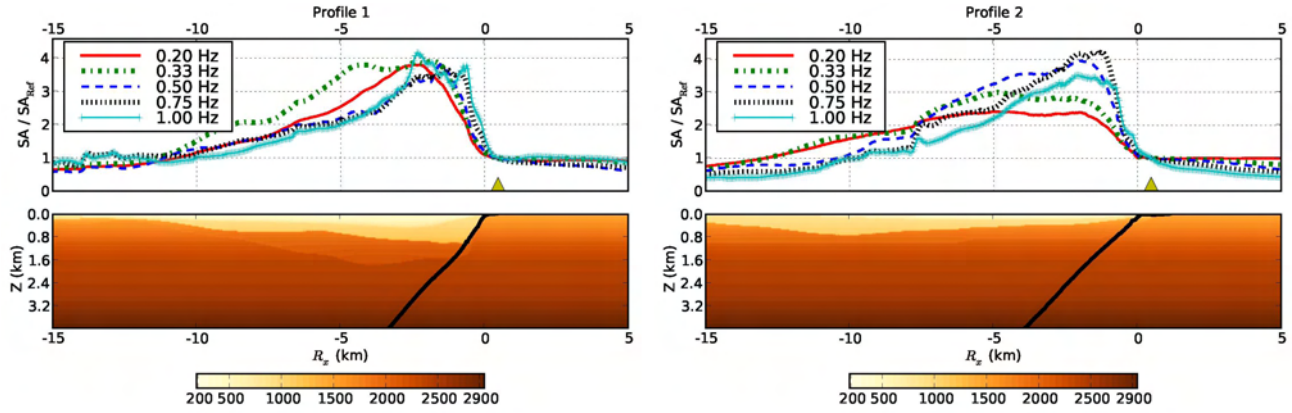

Figure 18: